



18 **Abstract:**

19 Nitrogen (N) in subducting slab resides in both sediments and altered oceanic crust (AOC). The  
20 extent of subduction-zone metamorphic devolatilization of N in these reservoirs determines the  
21 amount of remaining N for deep recycling. However, N behavior inside the subduction zone,  
22 particularly below the forearc region, remains poorly understood so far. Here, we studied the pillow-  
23 shaped epidote-blueschist facies meta-basalts (hereafter refer to as blueschists) in the Heilongjiang  
24 Complex in Northeast China, aiming to understand the N behavior during the early subduction stage.  
25 Results show that these blueschists contain N (13.9 to 122.6 ppm; average: 51.0 ppm) up to seven  
26 times higher than the AOC (including pillow lavas) entering global trenches (N < 19 ppm; average  
27 7 ppm). The N concentrations of the blueschists correlate with the Ba and Th concentrations,  
28 indicating that significant N enrichment of the blueschists took place inside the subduction zone in  
29 addition to small N enrichment on seafloor. The N concentrations and  $\delta^{15}\text{N}$  values of the blueschists  
30 show two distinct mixing trends, indicating that two types of ammonium ( $\text{NH}_4^+$ ) were added into  
31 the blueschists. One is characterized by relatively high abundance and positive  $\delta^{15}\text{N}$  value ( $\sim +3\text{‰}$ ),  
32 which can be attributed to the direct assimilation of  $\text{NH}_4^+$  in metamorphic fluids derived from the  
33 sedimentary components in the *mélange*. The other is characterized by relatively low abundance  
34 and extremely low  $\delta^{15}\text{N}$  values ( $\sim -16\text{‰}$ ). This  $\text{NH}_4^+$  is consistent with a product of abiotic  
35 reduction of sediment-derived  $\text{N}_2$ . This study demonstrates that the labile N in sediments released  
36 during early subduction can be at least partially (if not all) re-fixed into the more refractory meta-  
37 igneous part of the subducting slab, which facilitates the retention of N for deep subduction and  
38 recycling.

## 39 **1. Introduction**

40 Nitrogen (N) recycling across subduction zones is a critical part of geological N cycle on Earth  
41 (e.g., Hilton et al., 2002; Johnson and Goldblatt, 2015; Bekaert et al., 2020). Nitrogen in the surface  
42 reservoirs (e.g., the atmosphere, hydrosphere and biosphere) can be incorporated into seafloor  
43 sediments (by precipitation of organic matter and clay minerals) and altered oceanic crust (AOC;  
44 by hydrothermal and/or microbial alteration). The N concentrations of subducting sediments can  
45 vary depending on lithology from as low as ~ 10 ppm in sandstones, carbonates and cherts, to as  
46 high as ~2400 ppm in the organic-rich top sediments (e.g., Sadofsky and Bebout, 2004; Li and  
47 Bebout, 2005). In contrast, AOC commonly show much lower N concentrations in a range of 1.3-  
48 18.2 ppm (e.g., Busigny et al., 2005, 2019; Li et al., 2007; Bebout et al., 2018). Even though, AOC  
49 may contain a large N inventory at least of the same order of magnitude to the overlying sediments  
50 in the subducting slab because of its much larger volume (Li et al., 2007). Inside the subduction  
51 zones, part of the slab N may be released back to the surface by metamorphic devolatilization and  
52 restored in mantle wedge serpentinites by the infiltration of slab-derived fluids; the remainder will  
53 be subducted into the deep mantle (e.g., Hilton et al., 2002, 2010; Bebout et al., 2013; Pagé et al.,  
54 2018), which could be subsequently sampled by plume-related magmas (e.g., Dauphas and Marty,  
55 1999; Barry and Hilton, 2016; Halldórsson et al., 2016). Subduction-zone N recycling could thus  
56 have potentially impacted the long-term evolution of Earth's surface and interior reservoirs (e.g.,  
57 Sano et al., 2001; Marty and Dauphas, 2003; Mallik et al., 2018; Bekaert et al., 2020), which  
58 however cannot be quantitatively assessed so far because the important knowledge of N retention  
59 in the slab inside the subduction zones is not well understood.

60 Metamorphic rocks from ancient subduction zones provide a window to examine the N behavior  
61 in subduction zones (e.g., Haendel et al., 1986; Bebout and Fogel, 1992; Bebout, 1997; Busigny et  
62 al., 2003a; Sadofsky and Bebout, 2003; Jia, 2006; Halama et al., 2010; Li et al., 2014; Sievers et al.,  
63 2017). Nitrogen isotope ratio can be used as a robust tool to assess N devolatilization because of  
64 large magnitudes of isotope fractionations between minerals and the common devolatilized N  
65 species (NH<sub>3</sub> or N<sub>2</sub>; Li et al., 2021a, 2021b). In general, <sup>14</sup>N is preferentially taken by the released  
66 NH<sub>3</sub> or N<sub>2</sub>, which can result in progressive <sup>15</sup>N enrichment in the remaining rocks along prograde  
67 metamorphism (e.g., Haendel et al., 1986; Bebout and Fogel, 1992; Mingram and Bräuer, 2001).

68 Nitrogen devolatilization modeling of metasedimentary rocks subducted from the forearc to  
69 sub-arc depths in four ancient subduction zones suggested high-degree (~70%) N loss (in form of  
70 N<sub>2</sub>) in the Catalina Schist (Bebout and Fogel, 1992), medium-degree (~30%) N loss (in form of NH<sub>3</sub>)  
71 in the European Variscan (Mingram and Bräuer, 2001), and nearly no N loss in the Schistes Lustrés  
72 (Busigny et al., 2003a) and Franciscan Complex (Sadofsky and Bebout, 2003). These results imply  
73 that the fate of N in the subducted sediments could be strongly variable among different subduction  
74 zones, which is speculated to be dependent on the thermal structure of individual subduction zone  
75 (e.g., warm for the Catalina Schist vs. cold for the Schistes Lustrés; Busigny et al., 2003b; Bebout,  
76 2007a).

77 In contrast, studies on high-pressure (HP) to ultrahigh-pressure (UHP) eclogites observed little  
78 loss but retention of N in AOC to the sub-arc depth (Philippot et al., 2007; Halama et al., 2010, 2014;  
79 Busigny et al., 2011). This implies that AOC could be more resistant to metamorphic  
80 devolatilization than sediments. More interestingly, based on correlation of N and trace element  
81 concentrations, Halama et al. (2010) observed potential addition of sediment-derived N to the  
82 eclogites in the Raspas Complex (Ecuador) by fluid-rock interactions inside the subduction zone.  
83 Similarly, relatively high N concentrations (3-74 ppm) have also been observed in some high-  
84 pressure (HP) peridotites from the Central Alps, Raspas Complex (Ecuador) and Almirez Massif  
85 (Spain), which are speculated to be a result of admixing of sedimentary N during prograde  
86 metamorphism within the subduction zones (e.g., Halama et al., 2010, 2014; Cannà et al., 2020),  
87 although N addition during seafloor alteration is also possible. Nevertheless, these studies imply  
88 that part of the sedimentary N could be recaptured by the meta-igneous part of the subducting slab  
89 during prograde metamorphism. This process, if widely occurs inside the subduction zone, may play  
90 a critical role to promote the deep recycling of slab N. However, it is still unclear how common this  
91 process is inside the subduction zone, and in particular, whether it can occur in the forearc region  
92 where significant N devolatilization from sediments could be initiated (e.g., Bebout and Fogel,  
93 1992).

94 In this study, aiming to understand the N behavior in the early subduction stage in the forearc  
95 region, we investigated the N concentrations and isotope compositions, as well as major and trace  
96 elements of epidote-blueschist facies meta-basalts (hereafter refer to as blueschists) from the

97 Heilongjiang Complex in Northeast China (NE China). These blueschists still retain pillow shaped,  
98 which clearly indicates that their protoliths were from the topmost parts of ancient AOC. The  
99 epidote-blueschist facies metamorphism occurred in 198-175 Ma (see Zhou and Li, 2017 and  
100 reference therein) with peak metamorphic conditions of 320-450°C and a peak pressure of 0.9-  
101 1.1GPa (e.g., Zhou et al., 2009), which is equivalent to a subduction depth of ~40 km.

102

## 103 **2. Geological background and samples**

### 104 **2.1 Regional geology**

105 Northeast China is geologically comprised of several micro-continental blocks (**Fig. 1a**; Sengör  
106 et al., 1993; Jahn, 2004; Li, 2006). Its western part consists of the Songliao, Xing'an and Erguna  
107 blocks, which all belong to the Central Asian Orogenic Belt. These blocks mark the broad collision  
108 zone between the North China Craton in the south and the Siberian Craton in the north following  
109 the closure of the Paleo-Asian Ocean (Fig. 1a). Its eastern part consists of the Heilongjiang Complex  
110 in the west, the Jiamusi Block in the middle, and the Nadanhada Terrane in the east (Fig. 1b), which  
111 is a late Triassic-Cretaceous accretionary terrane formed by the westward subduction of the Paleo-  
112 Pacific Plate (e.g., Zhou et al., 2014).

113 The Heilongjiang Complex is an HP metamorphic belt over-thrusted onto the western margin  
114 of the Jiamusi Block along the north-south directed Mudanjiang Fault (F1 in Fig. 1b), which was  
115 later truncated by the Yilan-Yitong Fault (F2; Zhou et al., 2009; Zhou and Li, 2017). The HP  
116 Heilongjiang Complex is characterized by occurrence of blueschists, together with serpentinites,  
117 greenschist-facies marble, two-mica schists, muscovite-albite schists, quartz schists, quartzites and  
118 minor amphibolites (e.g., Li et al., 1999; Wu et al., 2007; Zhou and Li, 2017). Previous studies have  
119 identified that the Heilongjiang Complex was a tectonically juxtaposed mélangé (Wu et al., 2007;  
120 Zhou et al., 2009, 2010; Zhu et al., 2015, 2017) as a result of an east-west directed closure of an  
121 ancient ocean, which was likely related to the Paleo-Pacific Ocean (Li et al., 2021c).

122 The blueschists in the Heilongjiang Complex are mainly exposed in three areas, i.e., from south  
123 to north, Mudanjiang, Yilan, and Luobei (Fig. 1b). Most previous studies on the blueschists in the  
124 Heilongjiang Complex have been focused on the Mudanjiang and Yilan areas (e.g., Zhou et al., 2009;  
125 Zhu et al., 2015, 2017; Ge et al., 2017). The Luobei blueschist outcrops are relatively difficult to  
126 access and have not been well studied yet. The dating of detrital zircons gave the maximum protolith

127 ages of 288-258 Ma for the Yilan blueschists and 224-213 Ma for the Mudanjiang blueschists,  
128 respectively (Zhou et al., 2013; Ge et al., 2017). Ar-Ar and Rb-Sr dating of these blueschists gave  
129 the ages of the blueschist-facies metamorphism to be 198-175 Ma in these two places (Wu et al.,  
130 2007; Zhou et al., 2009, 2010, 2013; Zhou and Li, 2017).

## 131 **2.2 Sampling**

132 Twenty-seven blueschist samples were collected from the Mudanjiang (n = 13) and Yilan (n =  
133 14) areas for this study. The Mudanjiang blueschists commonly preserve pillow structure and occur  
134 as tectonic lens dominantly in greenschist-facies mica schist with locally preserved stratigraphic  
135 layers supporting a sedimentary origin (see Zhou et al., 2009; Zhu et al., 2015; Ge et al., 2016 for  
136 detail). The Yilan blueschists occur as small blocks, boudins or sheets that range from meters to  
137 hundreds of meters in length with well-preserved pillow structures, which spread in in greenschist-  
138 facies mica-schist (see Zhou et al., 2009; Zhu et al., 2015; Ge et al., 2016 for detail). All the samples  
139 for this study were collected from the inner parts of the pillows or lens. The rims of the pillow or  
140 lens and veins were carefully excluded to avoid retrograde metamorphic influence.

## 141 **2.3 Petrographic description**

142 The detailed petrographic descriptions of both the Mudanjiang and Yilan blueschists have been  
143 given by several previous studies in detail (Zhou et al., 2009; Zhu et al., 2015; Ge et al., 2016).  
144 Some key information is summarized here. Meta-basalts from the Mudanjiang area have the typical  
145 mineral assemblage of sodic amphibole (20-25%), albite (45%-50%), epidote (20-25%), phengite  
146 (5-10%) and chlorite (10-15%) (Fig. 2b and 2c). The sodic amphibole is small (0.5-1 mm; Fig. 2b)  
147 and its composition ranges from glaucophane to magnesio-riebeckite (Zhou et al., 2009). Chlorite  
148 occurs either in the matrix or around glaucophane (Fig. 2b). The schistosity is defined by sodic  
149 amphibole, epidote and chlorite (Fig. 2b and 2c). Few fluid inclusions (1  $\mu$ m to 5  $\mu$ m) were observed  
150 in some of the phengite but their overall abundance is low.

151 Meta-basalts from the Yilan area are dominantly characterized by the mineral assemblages of  
152 sodic amphibole (20-25%), albite (35%-40%), epidote (25-35%), phengite (5-10%) and chlorite  
153 (<10%). (Fig. 2). The sodic amphibole is small (0.5-1 mm; Fig. 2e and 2f) and its composition is  
154 dominated by ferro-glaucophane (Zhou et al., 2009; Ge et al., 2016). Chlorite occurs either in the  
155 matrix or around glaucophane and albite (Fig. 2f). The schistosity is defined by sodic amphibole,

156 epidote and chlorite (Fig. 2e and 2f). Few fluid inclusions (1  $\mu\text{m}$  to 5  $\mu\text{m}$ ) were observed in some of  
157 the phengite but their overall abundance is low.

158 Overall, the presence of glaucophane and ferro-glaucophane, associated with epidote and  
159 phengite, indicates epidote-blueschist facies metamorphism in the Yilan and Mudanjiang meta-  
160 basalts (Zhou et al., 2009). The presence of chlorite indicates these samples experienced retrograde  
161 metamorphism as well. However, the preservation of the high-Si signature (3.38-3.46 per formula  
162 unit) of phengite (Zhou et al., 2009) indicates that the retrograde metamorphic effect is relatively  
163 small on the meta-basalts.

164 .

### 165 **3. Analytical methods**

#### 166 **3.1 Whole-rock major and trace elements**

167 Blueschist rock samples were cleaned by removing surface material and further crushed and  
168 ground into fine powders (<200 mesh). Major and trace elements of eleven samples (i.e., the 15HLJ  
169 series; see Table 1) were analyzed in the Actlabs (Ontario, Canada) by a simultaneous/sequential  
170 Thermo Jarrell-Ash ENVIRO II ICP or a Varian Vista 735 ICP. Calibration was achieved using 12  
171 USGS and CANMET certified reference materials. The analytical errors are 0.5-5% of the absolute  
172 concentrations for major elements depending on abundance and 10% of the absolute concentrations  
173 for trace elements. Major and trace elements of the other sixteen samples (i.e., the 19HLJ and 20HLJ  
174 sample series; see Table 1) were analyzed at the State Key Laboratory of Continental Dynamics in  
175 Northwest University, Xi'an, China. Major elements were measured using a Rigaku RIX 2000 X-  
176 ray Fluorescence spectrometer (XRF). Repeated analyses of USGS (BCR-2) and Chinese national  
177 rock standards (GSR-1 and GSR-3) gave an analytical error better than 5% of the absolute  
178 concentrations for major elements (Wang and Liu, 2016). Trace elements concentrations were  
179 analyzed by an Agilent 7500a inductively coupled plasma mass spectrometry (ICP-MS). The  
180 analytical uncertainty is less than 10% of the absolute concentrations (Liu et al., 2007).

#### 181 **3.2 Whole-rock N concentrations and isotope compositions**

182 Nitrogen concentration and isotope composition of blueschists were analyzed by the offline  
183 sealed-tube combustion and extraction methods coupled with carrier-gas isotope ratio mass  
184 spectrometry. The analytical details have been described by Li et al. (2021d) and are briefly  
185 summarized here. Sample powders were loaded into a one-end sealed quartz tube together with

186 quartz wool and  $\text{Cu}_x\text{O}_x$  reagents. The tube was then put on a custom-made metal manifold to pump  
187 overnight, sealed under high vacuum, and combusted at  $1000^\circ\text{C}$  for 8 hours for a complete N  
188 extraction (Li et al., 2021d). The sample tube was then loaded back into the metal manifold and  
189 cracked under high vacuum. The released  $\text{N}_2$  was cryogenically purified and quantified by a  
190 capacitance manometer. After quantification, the  $\text{N}_2$  gas was carried by an ultrahigh-purity helium  
191 gas flow to a Thermo Finnegan MAT 253 isotope ratio mass spectrometer for N isotope analysis.  
192 All N isotope data were reported by the  $\delta$  notation, i.e.,  $\delta^{15}\text{N}_{\text{sample}} = \left(\frac{^{15}\text{N}/^{14}\text{N}}{^{15}\text{N}/^{14}\text{N}}\right)_{\text{sample}} / \left(\frac{^{15}\text{N}/^{14}\text{N}}{^{15}\text{N}/^{14}\text{N}}\right)_{\text{standard}} -$   
193 1, where the standard is atmospheric  $\text{N}_2$ . Based on repeated analyses of samples and two certified  
194 reference material, i.e., the low-organic content soil standard (reference values: N = 0.133 wt.%;  
195  $\delta^{15}\text{N} = +6.97\text{‰}$ ) and high-organic content sediment standard (reference values: N = 0.52 wt.%;  $\delta^{15}\text{N}$   
196 =  $+4.32\text{‰}$ ), the analytical error is better than 6% ( $2\sigma$ ) for N concentration and 0.2‰ ( $2\sigma$ ) for  $\delta^{15}\text{N}$ .

197

## 198 **4. Results**

### 199 **4.1 Major and trace elements**

200 Whole-rock major and trace element compositions of the Mudanjiang and Yilan blueschists are  
201 listed in Table 1. Overall, the blueschist samples have  $\text{SiO}_2$  concentrations from 39.81% to 52.32%,  
202 total FeO concentrations from 9.58% to 15.91%, MgO concentrations from 2.69% to 6.93%,  $\text{TiO}_2$   
203 concentrations from 1.57% to 4.56%, and  $\text{Na}_2\text{O}$  concentrations from 2.09% to 5.48%. Both the  
204 Mudanjiang and Yilan blueschist samples have high concentrations of rare earth elements (REE)  
205 with  $\Sigma\text{REE}$  varying from 52.2 to 196.6 ppm for the Mudanjiang blueschists and 104.4 to 295.3 ppm  
206 for the Yilan blueschists, respectively. On the diagram of chondrite-normalized REE patterns, the  
207 Mudanjiang blueschists show slight enrichments in light REE (LREE), with  $(\text{La}/\text{Yb})_{\text{N}}$  ratios of 2.5  
208 to 4.2 and  $(\text{La}/\text{Sm})_{\text{N}}$  ratios of 1.3 to 1.9, and relatively gentle right-dipping REE patterns similar to  
209 those of enriched mid-ocean ridge basalts (E-MORB; Fig. 3a). Most of the Yilan blueschists display  
210 strong enrichments in LREE, with  $(\text{La}/\text{Yb})_{\text{N}}$  ratios of 5.6 to 18.5 and  $(\text{La}/\text{Sm})_{\text{N}}$  ratios of 1.6 to 5.9,  
211 and steep right-dipping patterns similar to those of ocean island basalts (OIB; Fig. 3b). Three Yilan  
212 samples (15HLJ-39, 15HLJ-40 and 15HLJ-41) display flat distribution of LREE and strong  
213 depletion in heavy REE (HREE), with  $(\text{La}/\text{Yb})_{\text{N}}$  ratios of 26.4 to 28.5 and  $(\text{La}/\text{Sm})_{\text{N}}$  ratios of  $\sim 1.3$   
214 (Fig. 3b). The REE patterns of these three samples have been attributed to the low-degree partial  
215 melting of garnet-facies peridotites in which HREEs were retained in garnet in the residue (Zhu et



216 al., 2015). Nevertheless, consistent with previous studies (Zhou et al., 2009; Zhu et al., 2015; Ge et  
217 al., 2017), the overall REE patterns of the Yilan blueschists are indicative of an origin similar to  
218 OIB.

## 219 **4.2 N concentrations and isotope compositions**

220 The N concentrations and  $\delta^{15}\text{N}$  values of the blueschist samples from Mudanjiang and Yilan are  
221 listed in Table 1. The Mudanjiang blueschists display a large range in N concentrations from 13.9  
222 ppm to 83.6 ppm, but a relatively small  $\delta^{15}\text{N}$  range from  $-0.5\text{‰}$  to  $+3.7\text{‰}$  (Fig. 4). The Yilan  
223 blueschists show large variations in both N concentrations and  $\delta^{15}\text{N}$  values, which can be subdivided  
224 into two groups: group A samples are characterized by relatively high N concentrations (21.2 ppm  
225 to 122.6 ppm; average: 87.4 ppm) and positive  $\delta^{15}\text{N}$  values within a small range of  $+0.9\text{‰}$  to  $+3.2\text{‰}$   
226 (average:  $+2.5 \pm 0.7\text{‰}$ ;  $1\sigma$ ;  $n = 8$ ); whereas group B samples show relatively low N concentrations  
227 (17.3 ppm to 46.9 ppm; average: 33.9 ppm) and large  $\delta^{15}\text{N}$  variations with strikingly negative values  
228 ( $-3.3\text{‰}$  to  $-10.9\text{‰}$ ; Fig. 4). It should be noted that, the two sets of samples in group B with distinct  
229 REE patterns (Fig. 3b) show no difference in N concentrations and  $\delta^{15}\text{N}$  values: 17.3 to 39.7 ppm  
230 and  $-3.3\text{‰}$  to  $-10.1\text{‰}$  for samples with strong HREE depletion, 24.3 to 46.9 ppm and  $-3.8\text{‰}$  to  
231  $-10.9\text{‰}$  for the other group B samples, respectively. This indicates that their N signatures more  
232 likely reflect a secondary N rather than original magmatic N. Overall, the  $\delta^{15}\text{N}$  values of the  
233 blueschists from the Heilongjiang Complex overlap with those of basaltic portion of AOC from  
234 global oceans, but the N concentrations of the blueschists are significantly higher than those of  
235 global basaltic AOC ( $< 19$  ppm; Fig. 4).

236

## 237 **5. Discussions**

### 238 **5.1 Nitrogen residence in blueschist**

239 Fixed N in minerals is generally accepted to be in form of ammonium ( $\text{NH}_4^+$ ). Because of the  
240 similar ionic radius (IR) and charges between  $\text{K}^+$  (IR=1.64 Å; Shannon and Prewitt, 1969) and  $\text{NH}_4^+$   
241 (IR=1.67 Å; Sidey, 2016), N can be easily enriched into K-bearing minerals (e.g., micas and alkali  
242 feldspars; Yamamoto and Nakahira, 1966; Honma and Itihara, 1981; Bos et al., 1988). The  
243 substitution of  $\text{K}^+$  by  $\text{NH}_4^+$  has been well supported by the positive correlations between N and  $\text{K}_2\text{O}$   
244 concentrations observed in several metamorphic suites (e.g., Bebout, 1997; Busigny et al., 2003a;  
245 Busigny and Bebout, 2013; Sievers et al., 2017). Surprisingly, such a correlation has not been

246 observed in AOC (e.g., Li et al., 2007; Busigny et al., 2019). This may be attributed to more  
 247 complicated incorporation of N in AOC involving multiple secondary minerals (Staudigel, 2014)  
 248 and organic matter (Ménez et al., 2012) during alteration of oceanic crust. In addition,  $\text{NH}_4^+$  can  
 249 also be assimilated by  $\text{Na}^+$ - or  $\text{Ca}^{2+}$ -bearing minerals due to the similar ionic radius between  $\text{NH}_4^+$   
 250 and  $\text{Na}^+$  ( $\text{IR}=1.39 \text{ \AA}$ ; Shannon and Prewitt, 1969) and the replacement of  $\text{Ca}^{2+}+\text{Mg}^{2+}$  by  $\text{Al}^{3+}+\text{NH}_4^+$   
 251 (e.g., Honma and Itihara, 1981; Watenphul et al., 2010; Li et al., 2021d).

252 In the studied blueschists, the N concentrations do not correlate with  $\text{Na}_2\text{O}$  and  $\text{MgO}$   
 253 concentrations, but  $\text{K}_2\text{O}$  concentrations (Fig. 5). This suggests that most of N resides as  $\text{NH}_4^+$  in the  
 254 K-bearing minerals, which are dominated by phengite in the studied samples. Phengite has also been  
 255 demonstrated to be the major host mineral for N in rocks that have experienced HP and UHP  
 256 metamorphism (e.g., Li et al., 2014; Halama et al., 2017). In addition, few fluid inclusions observed  
 257 in the phengite crystals may also contain N but their contribution to the overall N concentrations of  
 258 blueschists should be small due to their minor abundance. Nevertheless, although some degree of  
 259 retrograde metamorphism has been observed in the samples (Fig. 2), the majority of N hosted by  
 260 phengite should not be significantly affected because of the good preservation of phengite (Zhou et  
 261 al., 2009).

## 262 **5.2 Effect of metamorphic devolatilization**

263 To assess the metamorphic devolatilization effect on the blueschist samples, we adopted the  
 264 method of Busigny et al. (2003a) by comparing the variations of multiple fluid-mobile elements  
 265 (e.g., K, Rb and Cs). This model is based on the different compatibilities among K, Rb and Cs during  
 266 devolatilization, in which Cs is most strongly fractionated into the fluids, followed by Rb and K  
 267 (Melzer and Wunder, 2000). The changes of K, Rb and Cs abundances through progressive  
 268 devolatilization can be described by Equation (1):

$$269 \quad R_{rock}^f = R_{rock}^0 \times F^{(1/K_D-1)} \quad (1)$$

270 where  $R_{rock}^0$  and  $R_{rock}^f$  represent the initial and final elemental ratios (e.g., Rb/K and Cs/Rb) of  
 271 rock before and after devolatilization, respectively.  $F$  is the fraction of element remaining in the  
 272 rock after devolatilization.  $K_D$  is the ratio of distribution coefficients for the Cs-Rb ( $K_D^{Cs-Rb}$ ) or  
 273 Rb-K ( $K_D^{Rb-K}$ ) system (Busigny et al., 2003a for detail). Considering that K, Rb, Cs and  $\text{NH}_4^+$   
 274 dominantly reside in K-bearing minerals (i.e., phengite in our case), elemental ratios among K, Rb,

275 Cs and  $\text{NH}_4^+$  in phengite largely reflect those of whole rock (Zack et al., 2001). Consequently,  
276  $K_D^{\text{Cs-Rb}}$  and  $K_D^{\text{Rb-K}}$  values of phengite are employed in the modeling (Table 2). It should be noted  
277 that the employed  $K_D^{\text{Cs-Rb}}$  and  $K_D^{\text{Rb-K}}$  values of phengite in the modeling are the data from  
278 experiments at 600 °C and 2 GPa (Table 2), which are so far the lowest temperature and pressure  
279 with available  $K_D$  values for phengite (Busigny et al., 2003a). Because the  $K_D^{\text{Cs-Rb}}$  and  $K_D^{\text{Rb-K}}$   
280 values of phengite decrease with decrease in temperature and pressure (Busigny et al., 2003a), their  
281 values at 320-450°C and 0.9-1.1 GPa for the studied blueschist (Zhou et al., 2009) would be smaller.  
282 Thus, the employment of data from high temperature and pressure in our modeling may cause some  
283 uncertainty, but it should not affect the semi-quantitative constraint on the devolatilization effect.  
284 On the diagram of molar abundances of Rb versus Cs (Fig. 6a) and K versus Rb (Fig. 6b), blueschists  
285 from Mudanjiang and Yilan are broadly distributed along a linear line instead of following the  
286 devolatilization trends illustrated by the dashed curves. This suggests that the effect of metamorphic  
287 devolatilization on these fluid-mobile elements is minor. To further examine the effect of  
288 metamorphic devolatilization on N, N/K molar ratios are plotted against  $\delta^{15}\text{N}$  values on Fig. 6c.  
289 Because  $^{15}\text{N}$  is more enriched in minerals than in  $\text{N}_2$  or  $\text{NH}_3$  (Li et al., 2021a, 2021b), metamorphic  
290 devolatilization would lead to a progressive decrease in the N/K ratio with increase in the  $\delta^{15}\text{N}$  value  
291 of the rocks (e.g., Bebout and Fogel, 1992; Mingram and Bräuer, 2001). However, this trend is not  
292 observed in the studied blueschists (Fig. 6c), which consistently suggests that the effect of  
293 metamorphic devolatilization on N in these blueschists is minor.

### 294 **5.3 Nitrogen enrichment in protoliths on seafloor**

295 It is noted that the protoliths of the blueschists from Mudanjiang (E-MORB) and Yilan (OIB)  
296 are different to normal mid-ocean ridge basalts (N-MORB; Zhou and Li, 2017; Fig. 3). As a result,  
297 the initial N inherited from their magmatic sources in these protoliths could be slightly different.  
298 Both fresh N-MORB and less contaminated E-MORB have  $\delta^{15}\text{N}$  values of  $\sim -3\text{‰}$  to  $-5\text{‰}$  (e.g.,  
299 Javoy and Pineau, 1991; Marty and Humbert, 1997; Marty and Zimmermann, 1999; Marty and  
300 Dauphas, 2003; Li et al., 2007). In contrast, OIB show highly variable  $\delta^{15}\text{N}$  values from  $-3\text{‰}$  to  
301  $+15\text{‰}$  (e.g., Exley et al., 1987; Marty and Dauphas, 2003; Halldórsson et al., 2016), which could  
302 be attributed to recycling of crustal N into their magmatic sources. Nevertheless, the initial N  
303 inherited from their magmatic sources should be very low in abundance ( $< 2$  ppm) due to the low

304 solubility of N in mafic magmas (Libourel et al., 2003). Consequently, their original magmatic N  
305 signature can be easily overprinted by addition of secondary N during seafloor weathering. Because  
306 the protoliths of all the studied blueschist samples were pillow basalts, they should have undergone  
307 low-temperature alterations on seafloor similar to those of the topmost part of global oceanic crust.  
308 Consequently, we can reasonably assume that the N concentrations and isotope signatures of the  
309 protoliths of the Mudanjiang and Yilan blueschists, despite their origin, should be similar to those  
310 of the upper section of AOC, which are commonly characterized by sedimentary-like positive  $\delta^{15}\text{N}$   
311 values (Fig. 4; Busigny et al., 2005, 2019; Li et al., 2007; Bebout et al., 2018), although some  
312 negative  $\delta^{15}\text{N}$  values were observed in the basalts of ODP sites 801 and 1149 as the availability of  
313 sedimentary N was diminished (Li et al., 2007).

#### 314 **5.4 Element remobilization inside the subduction zone**

##### 315 **5.4.1 Major and trace element evidence**

316 Besides seafloor alteration, fluid-rock interactions inside the subduction zone may also add N  
317 into the meta-igneous part of the slab (e.g., Halama et al., 2010, 2017). Some elements, such as Ba,  
318 U, Th and K, can be used to distinguish between these two processes (e.g., Bebout, 2007a, 2007b;  
319 Halama et al., 2010).

320 Fluid-rock interactions inside the subduction zone can result in greater enrichment of Ba than  
321 K in the rock, whereas seafloor alteration does the opposite (Bebout, 2007a, 2007b). Fig. 7a  
322 illustrates the comparison between Ba and K concentrations that are normalized to Th  
323 concentrations to remove the effect of magmatic fractional crystallization (e.g., Bebout, 2007a;  
324 Halama et al., 2010). The blueschist samples from the Heilongjiang Complex show higher Ba/Th  
325 ratios that deviate from the seafloor alteration trend defined by modern AOC (e.g., ODP Sites 801,  
326 1149 and 504) but are close to the metamorphic enrichment trend defined by high-grade eclogites  
327 (e.g., those from the Raspas Complex and Samana Peninsula; Sorensen et al., 1997; John et al., 2004;  
328 Halama et al., 2010). In addition, oceanic crust can assimilate significant amounts of U during  
329 seafloor alteration (Staudigel et al., 1996; Staudigel, 2014), which produces a steep trend in the  
330 Th/U and Th diagram (Fig. 7b). In contrast, the studied blueschists have high Th concentrations and  
331 high Th/U ratios, which display a trend opposite to the seafloor alteration trend but again consistent  
332 with the metamorphic enrichment trend defined by high-grade eclogites. Therefore, the Th

333 enrichment observed in these blueschists is likely indicative of reaction with HP metamorphic fluids,  
334 which has been observed in other HP and UHP metabasite blocks (Fig. 7b; e.g., Sorensen et al.,  
335 1997; Saha et al., 2005; also see data compilation in Bebout, 2007a, 2007b, 2013). In summary,  
336 major and trace elemental data of the studied blueschists show clear signatures of metasomatic  
337 overprint by HP metamorphic fluids inside the subduction zone.

#### 338 **5.4.2 Subduction-zone N enrichment in blueschists**

339 Resolving fluid-rock metasomatism inside the subduction zone from seafloor alteration in  
340 above discussions provides a framework to explain the N data. The N concentrations of the  
341 Mudanjiang blueschists and the Yilan-group A blueschists positively correlate with Ba (Fig. 8a) and  
342 Th concentrations (Fig. 8b). Since these Ba and Th enrichments are attributed to fluid-rock  
343 interactions inside the subduction zone (Bebout, 2007a, 2007b, 2013), the majority of N enrichment  
344 in these blueschists samples can be consistently considered to take place inside the subduction zone.  
345 Compared with the Yilan-group A blueschists, the Yilan-group B blueschists commonly show much  
346 lower Ba and Th concentrations, suggesting much less metasomatic effect on the group B  
347 blueschists. It should be noted that the group A and B samples occur randomly in the outcrops  
348 without specific distribution pattern. This indicates that the fluid-rock interaction inside the  
349 subduction zone is highly heterogeneous, consistent with observations from other subduction-zone  
350 mélangé settings (e.g., Breeding et al., 2004; Spandler et al., 2008). Nevertheless, the Yilan-group  
351 B blueschists are much richer in N than global AOC, indicating that these blueschists were able to  
352 assimilate significant amounts of N. Overall, the significantly higher N concentrations in blueschists  
353 relative to AOC may reflect that low-temperature alteration on seafloor is less efficient to enrich N,  
354 whereas the high-temperature and high-pressure conditions inside the subduction zone may promote  
355 more efficient N fixation into meta-igneous rocks (Fig. 4).

#### 356 **5.4.3 Source and mechanisms for N enrichment of blueschists**

357 To determine the N source and detailed mechanism for the N enrichment in the blueschists  
358 inside the subduction zone, we examined the relationship between the N concentrations and  $\delta^{15}\text{N}$   
359 values of the blueschists (Fig. 4). The Mudanjiang blueschists and the Yilan-group A blueschists  
360 show a  $\delta^{15}\text{N}$  range of  $-0.5\text{‰}$  to  $+3.7\text{‰}$ , falling into the isotope range ( $-0.9\text{‰}$  to  $+7.3\text{‰}$ ) of the top  
361 section of AOC which is considered to assimilate dissolved  $\text{NH}_4^+$  in seawater or derived from

362 overlying sediments (Busigny et al., 2005, 2019; Li et al., 2007). The high N concentrations (up to  
363 ~123 ppm) of the Mudanjiang blueschists and the Yilan-group A blueschists also require a source  
364 containing abundant N, consistent with sediments (e.g., Sadofsky and Bebout, 2004; Li and Bebout,  
365 2005). Consequently, N source of the Mudanjiang blueschists and the Yilan-group A blueschists can  
366 be attributed to the sedimentary component in the mélangé. This is also supported by the elevated  
367 Th and Ba concentrations in these blueschists (Figs. 7-8). The Mudanjiang and Yilan-group A  
368 blueschists have Ba/Th ratios of 25 to 421, consistent with those of clay-rich sedimentary rocks of  
369 21 to 458 but smaller than those of sedimentary carbonate of 700 to 2751 (Plank, 2014). This clearly  
370 points to a pelitic sedimentary source in mélangé, which is consistent with the field observation that  
371 blueschists of Heilongjiang Complex are closely associated pelitic mica schist (Zhou et al., 2009).

372       Employing a two-endmember mixing model (Li et al., 2007), the N concentrations and isotope  
373 compositions of the Mudanjiang blueschists and the Yilan-group A blueschists can be fitted by the  
374 addition of  $^{15}\text{N}$ -enriched  $\text{NH}_4^+$  with a  $\delta^{15}\text{N}$  value of +3‰ into rocks with an initial N concentration  
375 of about 14 ppm and a  $\delta^{15}\text{N}$  value of  $\sim +1\%$  (Fig. 4). This mixing trend could be interpreted by  
376 heterogeneous addition of sedimentary N into the protoliths of the blueschists with N of  $\sim 14$  ppm  
377 and  $\delta^{15}\text{N}$  of  $\sim +1\%$ . The mixing trend is still valid if consider that the protoliths of blueschists had  
378 heterogeneous N concentrations and isotope compositions similar to the upper branch of data of  
379 ODP Sites 801 and 1149 samples (Li et al., 2007; **Fig. 4**). In a simplified scenario of heterogeneous  
380 addition of sedimentary  $\text{NH}_4^+$  with  $\delta^{15}\text{N}$  value of +3‰ into the protoliths of the blueschists with  
381 relatively homogenous N ( $\sim 14$  ppm and  $\sim +1\%$ ), this gives  $\delta^{15}\text{N}$  value of +2.0‰ to +2.2‰ for  
382 sediment-derived dissolved  $\text{NH}_4^+$  in fluids employing the isotope fractionation of +1.0‰ to +0.8‰  
383 (Li et al., 2021b) between phengite and dissolved  $\text{NH}_4^+$  in fluids at temperature condition (320-450  
384 °C; Zhou et al., 2009) of epidote-blueschist facies metamorphism. Furthermore, a mass-balance  
385 calculation suggests that 36-89% of N (corresponding to 7.9-109.1 ppm N) in the Mudanjiang and  
386 Yilan-group A blueschists could come from sedimentary  $\text{NH}_4^+$  (Fig. 4).

387       The Yilan-group B blueschists all have negative  $\delta^{15}\text{N}$  values as low as  $\sim -11\%$ , apparently  
388 different from those of subducting sediments ( $+5.2 \pm 1.6\%$ ; see data complication in Li et al., 2014).  
389 Instead, the Yilan-group B data can be fitted by addition of  $^{15}\text{N}$ -depleted  $\text{NH}_4^+$  with a  $\delta^{15}\text{N}$  value of  
390  $\sim -16\%$  (Fig. 4). Notably, a similar  $^{15}\text{N}$ -depleted  $\text{NH}_4^+$  source has been observed in the ODP sites

391 801 and 1149 basalts (Li et al., 2007) and the UHP rocks with hydrothermally altered protoliths  
392 from the Sulu belt in eastern China (Li et al., 2014). An abiotic reduction of  $N_2$  to  $NH_4^+$  by  $Fe^{2+}$ -  
393 bearing minerals associated with kinetic isotope fractionation has been proposed to account for the  
394 formation of this extremely  $^{15}N$ -depleted  $NH_4^+$  (Li et al., 2007, 2014). Although abiotic  $N_2$  reduction  
395 in these cases occur before subduction, it does not preclude the occurrence of abiotic  $N_2$  reduction  
396 inside the subduction zone if favorable conditions to the reaction are met. In mafic rocks such as the  
397 studied blueschists,  $Fe(II)$  is abundant and can act as an efficient reductant to abiotically reduce  $N_2$   
398 at 300-500 °C and high-pressure conditions (Brandes et al., 1998; Li et al., 2014). Therefore, we  
399 consistently employ this mechanism to account for the  $^{15}N$ -depleted  $NH_4^+$  endmember ( $-16\%$ ) in  
400 the Yilan-group B blueschists, which is equivalent to a  $\delta^{15}N$  value of  $-15.0\%$  to  $-15.2\%$  for  
401 dissolved  $NH_4^+$  in fluids considering the isotope fractionation of  $+1.0\%$  to  $+0.8\%$  between phengite  
402 and dissolved  $NH_4^+$  in fluids at 320-450 °C (Li et al., 2021b). Although  $N_2$  inside the subduction  
403 zone could come from both metamorphic devolatilization of sediments (e.g., Bebout and Fogel,  
404 1992) and partial melting of the mantle wedge, the latter is unlikely to occur given the low-temperature  
405 conditions (320-450 °C) for the formation of the blueschists in the Heilongjiang Complex. Therefore,  
406 the enriched N in the Yilan-group B blueschists should be still sourced from the ambient sediment  
407 components in the *mélange*. At 320-450 °C, the  $\delta^{15}N$  difference between dissolved  $NH_4^+$  and  $N_2$  in  
408 fluids released from the sedimentary source with same N isotope composition is  $+5.6\%$  to  $+4.2\%$   
409 (Li et al., 2021a), which implies that the  $\delta^{15}N$  value of dissolved  $N_2$  in fluids is  $-3.6\%$  to  $-2.0\%$ .  
410 This requires a kinetic isotope fractionation of  $-11.4\%$  to  $-13.2\%$  between the product  $NH_4^+$  and  
411  $N_2$  in fluids, which is consistent with the kinetic isotope fractionation of  $-11\%$  to  $-16\%$  for abiotic  
412  $N_2$  reduction observed in previous studies (Li et al., 2007, 2014). Accordingly, a mass-balance  
413 calculation suggests that a minimum of 19-72% of N (corresponding to 3.3-36.0 ppm N) in the  
414 Yilan-group B blueschists could come from abiotic  $N_2$  reduction (Fig. 4).

415 The local oxygen fugacity may vary strongly at a small scale in the *mélange* zone (Tumiati et  
416 al., 2015), which could result in coexistence of  $N_2$  and  $NH_4^+$  in subduction-zone fluids (e.g., Jackson  
417 et al., 2021) although the relative abundances of  $N_2$  and  $NH_4^+$  in fluids could be highly variable.  
418 This could induce different N-fixation mechanisms between the Mudanjiang and Yilan-group A  
419 blueschists (i.e., direct  $NH_4^+$  assimilation) and the Yilan-group B blueschists (abiotic  $N_2$  reduction

420 to  $\text{NH}_4^+$ ). The Mudanjiang and Yilan-group A blueschists were likely able to access abundant fluids  
421 that have been interacted with sediments (Fig. 9), as revealed by their significantly elevated Ba, Th  
422 and N concentrations (Fig. 8), which favors direct  $\text{NH}_4^+$  assimilation. In contrast, the relatively low  
423 Ba, Th and N concentrations of the Yilan-group B blueschists indicate that the fluids reacted with  
424 these blueschists contained much less Ba, Th and  $\text{NH}_4^+$ , likely due to interactions with other  
425 blueschists along their flow path. The lack of  $\text{NH}_4^+$  in fluids made  $\text{N}_2$  contribute dominantly to  
426 blueschists through abiotic  $\text{N}_2$  reduction (Fig. 9), although this reaction is less efficient in supplying  
427  $\text{NH}_4^+$ . Consequently, the Yilan-group B blueschists gained relatively less amounts of  $\text{NH}_4^+$  with  
428 strong  $^{15}\text{N}$  depletion.

#### 429 **5.4.4 Implications to N recycling in subduction zones**

430 The discussion above demonstrates that the devolatilized sedimentary N (either in form of  $\text{NH}_4^+$   
431 or  $\text{N}_2$ ) can be at least partially re-fixed by the meta-igneous components of subducting slab inside  
432 the subduction zone. This process can transfer N from susceptible sediments to more refractory  
433 meta-igneous components in the *mélange* at the early stage of subduction.

434 *Mélange* is a common feature of modern-style subduction zones (Nielsen and Marschall, 2017).  
435 Field studies on the exhumed HP *mélange* zones have suggested that the thickness of *mélange* zones  
436 could vary from hundreds of meters to several kilometers (Bebout, 1991; Marschall et al., 2006).  
437 The low-seismic-velocity materials on the upper part of several modern subduction zones (Abers,  
438 2005), which possibly represent the *mélange* material, vary from 1 to 10 km in thickness (Marschall  
439 and Schumacher, 2012). If we assume that the *mélange* is composed of subducting sediments with  
440 an initial weighted average N concentration of 299 ppm (Sadofsky and Bebout, 2004; Li and Bebout,  
441 2005) and AOC with an initial weighted average N concentration of 7 ppm (Li et al., 2007; Bebout  
442 et al., 2018; Busigny et al., 2019), a ballpark estimate on the N re-fixation efficiency (i.e., the  
443 fraction of the devolatilized sedimentary N that can be re-fixed by the igneous components in the  
444 *mélange*) is illustrated in Fig. 10. The modeling results show that the re-fixation efficiency is  
445 strongly controlled by the relative thickness between sediments and AOC that are incorporated into  
446 the *mélange* zone (Fig. 10). Taking the modern Circum-Pacific subduction zones (representing ~70%  
447 of global subduction zones in length) as an example, even applying the maximum degree of  
448 sedimentary N loss (~40%; Bebout and Fogel, 1992; Bebout et al., 1999) during the epidote-



449 blueschist metamorphism in the Catalina Schist (an exceptionally hot subduction zone), the released  
450 N from the sediments (average thickness: 794 m) can be efficiently re-fixed if the mélange  
451 contains >850-meter AOC (Fig. 10). The required thickness of AOC for efficient re-fixation of  
452 devolatilized sedimentary N is even smaller to account for the diminished N devolatilization in cold  
453 subduction zones with geotherm of 8°C/km (Busigny et al., 2003a), which may be the case for most  
454 of modern subduction zones (Penniston-Dorland et al., 2015). It should be noted here that our  
455 modeling of the AOC thickness is conservative because (i) samples in this study were from inner  
456 parts of pillow basalts, which likely have experienced less degree of metasomatism than the rims of  
457 the pillows, and thus less degree of N enrichment; (ii) the devolatilized sedimentary N could also  
458 be re-fixed by the meta-peridotites of subducting slab or serpentinites in the mantle wedge (Halama  
459 et al., 2014; Pagé et al., 2018; Cannaò et al., 2020), which are also common components of mélange  
460 in subduction zones (e.g., Spandler et al., 2008) but not considered in our modeling due to the loose  
461 constraints of N characteristics on these components. Incorporating these parameters can further  
462 reduce the thickness of AOC required to re-fix the devolatilized sedimentary N. In turn, the meta-  
463 igneous components in the mélange in most of subduction zones can efficiently re-fix the  
464 devolatilized sedimentary N.

465 The K-bearing phases, such as phengite, are the major host of N in metamorphosed AOC (e.g.,  
466 blueschists, eclogites). Attributed to the stability of phengite over large temperature and pressure  
467 ranges (up to ~300 km) in subduction zones (Poli and Schmidt, 1995; Schmidt, 1996; Watenphul et  
468 al., 2010), N can be well retained beyond the sub-arc depth. Although some degrees of N loss from  
469 phengite may occur during further prograde metamorphism (Halama et al., 2017), significant  
470 amounts of N have been observed in the phengite in the UHP eclogites from the Sulu belt (eastern  
471 China), which has been subducted to >120 km or even > 200 km (Xu et al., 1992; Ye et al., 2000).  
472 This suggests that N can be well retained and recycled into the deep mantle.

473

## 474 **6. Conclusions**

475 The pillow-shaped blueschists in Northeast China provide a good opportunity to examine the  
476 N behavior at the early stage of subduction. These blueschists contain N concentrations seven times  
477 in average higher than AOC. The concentration correlations between N and other elements, such as

478 Ba, Th, indicate that most of the N in the blueschists was added inside the subduction zone. The  
479 relationship between the N concentrations and  $\delta^{15}\text{N}$  values of these blueschist indicates that two  
480 types of  $\text{NH}_4^+$  was added to the studied blueschists. The first type of  $\text{NH}_4^+$  is characterized by a  
481 positive  $\delta^{15}\text{N}$  value, likely directly derived from devolatilization of sediments. This type of N is  
482 significantly enriched in the blueschists that have undergone intensive interaction with metamorphic  
483 fluid. The other type of  $\text{NH}_4^+$  is characterized by strong  $^{15}\text{N}$  depletion, likely generated by abiotic  
484 reduction of sediment-derived  $\text{N}_2$ . This type of N is enriched in the blueschists that have undergone  
485 limited interaction with metamorphic fluid. These results show that the meta-igneous components  
486 of the slab can efficiently re-fix the devolatilized N from the sedimentary portion of the slab, which  
487 facilitates the retention of slab N for deep subduction and recycling.

488

#### 489 **Declaration of Competing Interest**

490 The authors declare that they have no known competing financial interests or personal  
491 relationships that could have appeared to influence the work reported in this paper.

492

#### 493 **Acknowledgements**

494 The research was funded by the National Natural Science Foundation of China (grant number:  
495 41730210) to J.-B.Z, and the Faculty Research Grant from China Institute of University of Alberta  
496 and NSERC-Discovery Grant to L.L. Authors are grateful to Dr. Porcelli for the editorial handling  
497 of the manuscript, and constructive comments from Dr. Ralf Halama, an anonymous reviewer and  
498 the special issue guest editors.

499

500 **References**

- 501 Abers, G.A., 2005. Seismic low-velocity layer at the top of subducting slabs: observations, predictions,  
502 and systematics. *Phys. Earth Planet. Inter.* 149(1), 7-29.  
503 <https://doi.org/10.1016/j.pepi.2004.10.002>
- 504 Bach, W., Peucker-Ehrenbrink, B., Hart, S.R., Blusztajn, J.S., 2003. Geochemistry of hydrothermally  
505 altered oceanic crust: DSDP/ODP Hole 504B – Implications for seawater-crust exchange  
506 budgets and Sr- and Pb-isotopic evolution of the mantle. *Geochem. Geophys. Geosyst.* 4(3).  
507 <https://doi.org/10.1029/2002GC000419>
- 508 Barry, P., Hilton, D., 2016. Release of subducted sedimentary nitrogen throughout Earth’s mantle.  
509 *Geochem. Perspect. Lett.* 2(2). <http://doi:10.7185/geochemlet.1615>
- 510 Bebout, G.E., 1991. Field-Based Evidence for Devolatilization in Subduction Zones: Implications for  
511 Arc Magmatism. *Science* 251(4992), 413-416. <https://doi.org/10.1126/science.251.4992.413>
- 512 Bebout, G.E., Fogel, M.L., 1992. Nitrogen-isotope compositions of metasedimentary rocks in the  
513 Catalina Schist, California: implications for metamorphic devolatilization history. *Geochim.*  
514 *Cosmochim. Acta* 56(7), 2839-2849. [https://doi.org/10.1016/0016-7037\(92\)90363-N](https://doi.org/10.1016/0016-7037(92)90363-N)
- 515 Bebout, G.E., 1997. Nitrogen isotope tracers of high-temperature fluid-rock interactions: Case study of  
516 the Catalina Schist, California. *Earth Planet Sci. Lett.* 151(1-2), 77-90.  
517 [https://doi.org/10.1016/S0012-821X\(97\)00117-9](https://doi.org/10.1016/S0012-821X(97)00117-9)
- 518 Bebout, G.E., Ryan, J.G., Leeman, W.P., Bebout, A.E., 1999. Fractionation of trace elements by  
519 subduction-zone metamorphism—effect of convergent-margin thermal evolution. *Earth Planet*  
520 *Sci. Lett.* 171(1), 63-81. [https://doi.org/10.1016/S0012-821X\(99\)00135-1](https://doi.org/10.1016/S0012-821X(99)00135-1)
- 521 Bebout, G.E., 2007a. Metamorphic chemical geodynamics of subduction zones. *Earth Planet Sci. Lett.*  
522 260(3), 373-393. <https://doi.org/10.1016/j.epsl.2007.05.050>
- 523 Bebout, G.E., 2007b. 3.20 - Trace Element and Isotopic Fluxes/Subducted Slab. In: Holland, H.D.,  
524 Turekian, K.K. (Eds.), *Treatise on Geochemistry*. Pergamon, Oxford, pp. 1-50.  
525 <https://doi.org/10.1016/B978-008043751-4/00231-5>
- 526 Bebout, G.E., Fogel, M.L., Cartigny, P., 2013. Nitrogen: Highly volatile yet surprisingly compatible.  
527 *Elements* 9(5), 333-338. <https://doi.org/10.2113/gselements.9.5.333>
- 528 Bebout, G.E., 2013. Metasomatism in subduction zones of subducted oceanic slabs, mantle wedges, and  
529 the slab-mantle interface, *Metasomatism and the Chemical Transformation of Rock*. Springer,  
530 pp. 289-349. [https://doi.org/10.1007/978-3-642-28394-9\\_9](https://doi.org/10.1007/978-3-642-28394-9_9)
- 531 Bebout, G.E., Penniston-Dorland, S.C., 2016. Fluid and mass transfer at subduction interfaces—The field  
532 metamorphic record. *Lithos* 240-243, 228-258. <https://doi.org/10.1016/j.lithos.2015.10.007>
- 533 Bebout, G.E., Banerjee, N., Izawa, M., Kobayashi, K., Lazzeri, K., Ranieri, L., Nakamura, E., 2018.  
534 Nitrogen concentrations and isotopic compositions of seafloor-altered terrestrial basaltic glass:  
535 implications for astrobiology. *Astrobiology* 18(3), 330-342.  
536 <https://doi.org/10.1089/ast.2017.1708>
- 537 Bekaert, D., Turner, S., Broadley, M., Barnes, J., Halldórsson, S., Labidi, J., Wade, J., Walowski, K.,  
538 Barry, P., 2020. Subduction-Driven Volatile Recycling: A Global Mass Balance. *Annu. Rev.*  
539 *Earth Planet. Sci.* 49, 2021. <https://doi.org/10.1146/annurev-earth-071620-055024>
- 540 Bos, A., Duit, W., van der Eerden, A.M., Jansen, J.B.H., 1988. Nitrogen storage in biotite: An  
541 experimental study of the ammonium and potassium partitioning between 1M-phlogopite and  
542 vapour at 2 kb. *Geochim. Cosmochim. Acta* 52(5), 1275-1283. [https://doi.org/10.1016/0016-7037\(88\)90281-5](https://doi.org/10.1016/0016-7037(88)90281-5)
- 543

544 Brandes, J.A., Boctor, N.Z., Cody, G.D., Cooper, B.A., Hazen, R.M., Yoder Jr, H.S., 1998. Abiotic  
545 nitrogen reduction on the early Earth. *Nature* 395(6700), 365. <https://doi.org/10.1038/26450>

546 Breeding, C.M., Ague, J.J., Bröcker, M., 2004. Fluid–metasedimentary rock interactions in subduction-  
547 zone mélange: Implications for the chemical composition of arc magmas. *Geology* 32(12),  
548 1041-1044. <https://doi.org/10.1130/G20877.1>

549 Busigny, V., Cartigny, P., Philippot, P., Ader, M., Javoy, M., 2003a. Massive recycling of nitrogen and  
550 other fluid-mobile elements (K, Rb, Cs, H) in a cold slab environment: evidence from HP to  
551 UHP oceanic metasediments of the Schistes Lustrés nappe (western Alps, Europe). *Earth Planet  
552 Sci. Lett.* 215(1-2), 27-42. [https://doi.org/10.1016/S0012-821X\(03\)00453-9](https://doi.org/10.1016/S0012-821X(03)00453-9)

553 Busigny, V., Cartigny, P., Philippot, P., Javoy, M., 2003b. Nitrogen recycling in subduction zones: A  
554 strong geothermal control. *Geochim. Cosmochim. Acta* 67(suppl 1), A51.

555 Busigny, V., Laverne, C., Bonifacie, M., 2005. Nitrogen content and isotopic composition of oceanic  
556 crust at a superfast spreading ridge: a profile in altered basalts from ODP Site 1256, Leg 206.  
557 *Geochem. Geophys. Geosyst.* 6(12). <https://doi.org/10.1029/2005GC001020>

558 Busigny, V., Cartigny, P., Philippot, P., 2011. Nitrogen isotopes in ophiolitic metagabbros: A re-evaluation  
559 of modern nitrogen fluxes in subduction zones and implication for the early Earth atmosphere.  
560 *Geochim. Cosmochim. Acta* 75(23), 7502-7521. <https://doi.org/10.1016/j.gca.2011.09.049>

561 Busigny, V., Bebout, G.E., 2013. Nitrogen in the silicate Earth: Speciation and isotopic behavior during  
562 mineral–fluid interactions. *Elements* 9(5), 353-358. <https://doi.org/10.2113/gselements.9.5.353>

563 Busigny, V., Cartigny, P., Laverne, C., Teagle, D., Bonifacie, M., Agrinier, P., 2019. A re-assessment of  
564 the nitrogen geochemical behavior in upper oceanic crust from Hole 504B: Implications for  
565 subduction budget in Central America. *Earth Planet Sci. Lett.* 525, 115735.  
566 <https://doi.org/10.1016/j.epsl.2019.115735>

567 Cannaò, E., Tiepolo, M., Bebout, G., Scambelluri, M., 2020. Into the deep and beyond: Carbon and  
568 nitrogen subduction recycling in secondary peridotites. *Earth Planet Sci. Lett.* 543, 116328.  
569 <https://doi.org/10.1016/j.epsl.2020.116328>

570 Clift, P., 2017. A revised budget for Cenozoic sedimentary carbon subduction. *Rev. Geophys.* 55, 97-125.  
571 <https://doi.org/10.1002/2016RG000531>

572 Dauphas, N., Marty, B., 1999. Heavy Nitrogen in Carbonatites of the Kola Peninsula: A Possible  
573 Signature of the Deep Mantle. *Science* 286(5449), 2488-2490.  
574 <http://10.1126/science.286.5449.2488>

575 Exley, R.A., Boyd, S.R., Matthey, D.P., Pillinger, C.T., 1987. Nitrogen isotope geochemistry of basaltic  
576 glasses: implications for mantle degassing and structure? *Earth Planet Sci. Lett.* 81(2), 163-174.  
577 [https://doi.org/10.1016/0012-821X\(87\)90153-1](https://doi.org/10.1016/0012-821X(87)90153-1)

578 Gale, A., Dalton, C.A., Langmuir, C.H., Su, Y., Schilling, J.G., 2013. The mean composition of ocean  
579 ridge basalts. *Geochem. Geophys. Geosyst.* 14(3), 489-518.  
580 <https://doi.org/10.1029/2012GC004334>

581 Ge, M.H., Zhang, J.J., Liu, K., Ling, Y.Y., Wang, M., Wang, J.M., 2016. Geochemistry and  
582 geochronology of the blueschist in the Heilongjiang Complex and its implications in the late  
583 Paleozoic tectonics of eastern NE China. *Lithos* 261, 232-249.  
584 <https://doi.org/10.1016/j.lithos.2015.11.019>

585 Ge, M.H., Zhang, J.J., Li, L., Liu, K., Ling, Y.Y., Wang, J.M., Wang, M., 2017. Geochronology and  
586 geochemistry of the Heilongjiang Complex and the granitoids from the Lesser Xing'an-  
587 Zhangguangcai Range: Implications for the late Paleozoic-Mesozoic tectonics of eastern NE

588 China. *Tectonophysics* 717, 565-584. <https://doi.org/10.1016/j.tecto.2017.09.004>

589 Haendel, D., Mühle, K., Nitzsche, H.-M., Stiehl, G., Wand, U., 1986. Isotopic variations of the fixed  
590 nitrogen in metamorphic rocks. *Geochim. Cosmochim. Acta* 50(5), 749-758.  
591 [https://doi.org/10.1016/0016-7037\(86\)90351-0](https://doi.org/10.1016/0016-7037(86)90351-0)

592 Halama, R., Bebout, G.E., John, T., Schenk, V., 2010. Nitrogen recycling in subducted oceanic  
593 lithosphere: the record in high-and ultrahigh-pressure metabasaltic rocks. *Geochim.  
594 Cosmochim. Acta* 74(5), 1636-1652. <https://doi.org/10.1016/j.gca.2009.12.003>

595 Halama, R., Bebout, G.E., John, T., Scambelluri, M., 2014. Nitrogen recycling in subducted mantle rocks  
596 and implications for the global nitrogen cycle. *Int. J. Earth Sci.* 103(7), 2081-2099.  
597 <https://doi.org/10.1007/s00531-012-0782-3>

598 Halama, R., Bebout, G.E., Marschall, H.R., John, T., 2017. Fluid-induced breakdown of white mica  
599 controls nitrogen transfer during fluid-rock interaction in subduction zones. *Int. Geol. Rev.*  
600 59(5-6), 702-720. <https://doi.org/10.1080/00206814.2016.1233834>

601 Halldórsson, S.A., Hilton, D.R., Barry, P.H., Füre, E., Grönvold, K., 2016. Recycling of crustal material  
602 by the Iceland mantle plume: New evidence from nitrogen elemental and isotope systematics of  
603 subglacial basalts. *Geochim. Cosmochim. Acta* 176, 206-226.  
604 <https://doi.org/10.1016/j.gca.2015.12.021>

605 Han, W., Zhou, J.-B., Wilde, S.A., Li, L., 2020. LA-ICPMS zircon U–Pb dating of the Heilongjiang  
606 Complex in the Luobei area: New constraints for the late Palaeozoic-Mesozoic tectonic  
607 evolution of Jiamusi Block, NE China. *Geol. J.* 55(3), 1644-1669.  
608 <https://doi.org/10.1002/gj.3443>

609 Hilton, D.R., Fischer, T.P., Marty, B., 2002. Noble gases and volatile recycling at subduction zones. *Rev.  
610 Mineral. Geochem.* 47(1), 319-370. <https://doi.org/10.2138/rmg.2002.47.9>

611 Honma, H., Itihara, Y., 1981. Distribution of ammonium in minerals of metamorphic and granitic rocks.  
612 *Geochim. Cosmochim. Acta* 45(6), 983-988. [https://doi.org/10.1016/0016-7037\(81\)90122-8](https://doi.org/10.1016/0016-7037(81)90122-8)

613 Jackson, C.R., Cottrell, E., Andrews, B., 2021. Warm and oxidizing slabs limit ingassing efficiency of  
614 nitrogen to the mantle. *Earth Planet Sci. Lett.* 553, 116615.  
615 <https://doi.org/10.1016/j.epsl.2020.116615>

616 Jahn, B.M., 2004. The Central Asian Orogenic Belt and growth of the continental crust in the Phanerozoic.  
617 *Geol. Soc. Spec. Publ.* 226(1), 73-100. <https://doi.org/10.1144/GSL.SP.2004.226.01.05>

618 Javoy, M., Pineau, F., 1991. The volatiles record of a “popping” rock from the Mid-Atlantic Ridge at 14  
619 N: chemical and isotopic composition of gas trapped in the vesicles. *Earth Planet Sci. Lett.*  
620 107(3-4), 598-611. [https://doi.org/10.1016/0012-821X\(91\)90104-P](https://doi.org/10.1016/0012-821X(91)90104-P)

621 Jia, Y., 2006. Nitrogen isotope fractionations during progressive metamorphism: A case study from the  
622 Paleozoic Cooma metasedimentary complex, southeastern Australia. *Geochim. Cosmochim.  
623 Acta* 70(20), 5201-5214. <https://doi.org/10.1016/j.gca.2006.08.004>

624 John, T., Scherer, E.E., Haase, K., Schenk, V., 2004. Trace element fractionation during fluid-induced  
625 eclogitization in a subducting slab: trace element and Lu–Hf–Sm–Nd isotope systematics. *Earth  
626 Planet Sci. Lett.* 227(3), 441-456. <https://doi.org/10.1016/j.epsl.2004.09.009>

627 Johnson, B., Goldblatt, C., 2015. The nitrogen budget of Earth. *Earth-Sci. Rev.* 148, 150-173.  
628 <https://doi.org/10.1016/j.earscirev.2015.05.006>

629 Johnson, H.P., Pruis, M.J., 2003. Fluxes of fluid and heat from the oceanic crustal reservoir. *Earth Planet  
630 Sci. Lett.* 216(4), 565-574. [https://doi.org/10.1016/S0012-821X\(03\)00545-4](https://doi.org/10.1016/S0012-821X(03)00545-4)

631 Kelley, K.A., Plank, T., Ludden, J., Staudigel, H., 2003. Composition of altered oceanic crust at ODP

632 Sites 801 and 1149. *Geochem. Geophys. Geosyst.* 4(6). <https://doi.org/10.1029/2002GC000435>

633 Li, G.Y., Zhou, J.B., Li, L., 2021c. A new tectonic framework for the composite orogenic metallogenic  
634 systems in the east of North China: The role of the Heilongjiang Ocean in the Late Paleozoic to  
635 Mesozoic. *Ore Geol. Rev.* 136, 104293. <https://doi.org/10.1016/j.oregeorev.2021.104293>

636 Li, J., Niu, B., Song, B., Xu, W., Zhang, Y., Zhao, Z., 1999. Crustal formation and evolution of northern  
637 Changbai Mountains, northeast China. Geological Publishing House, Beijing (in Chinese with  
638 English abstract) 1-137.

639 Li, J.Y., 2006. Permian geodynamic setting of Northeast China and adjacent regions: closure of the Paleo-  
640 Asian Ocean and subduction of the Paleo-Pacific Plate. *J. Asian Earth Sci.* 26(3), 207-224.  
641 <https://doi.org/10.1016/j.jseaes.2005.09.001>

642 Li, L., Bebout, G.E., 2005. Carbon and nitrogen geochemistry of sediments in the Central American  
643 convergent margin: insights regarding subduction input fluxes, diagenesis, and  
644 paleoproductivity. *J. Geophys. Res: Solid Earth* 110(B11).  
645 <https://doi.org/10.1029/2004JB003276>

646 Li, L., Bebout, G.E., Idleman, B.D., 2007. Nitrogen concentration and  $\delta^{15}\text{N}$  of altered oceanic crust  
647 obtained on ODP Legs 129 and 185: insights into alteration-related nitrogen enrichment and the  
648 nitrogen subduction budget. *Geochim. Cosmochim. Acta* 71, 2344-2360.  
649 <https://doi.org/10.1016/j.gca.2007.02.001>

650 Li, L., Zheng, Y.F., Cartigny, P., Li, J., 2014. Anomalous nitrogen isotopes in ultrahigh-pressure  
651 metamorphic rocks from the Sulu orogenic belt: Effect of abiotic nitrogen reduction during  
652 fluid-rock interaction. *Earth Planet Sci. Lett.* 403, 67-78.  
653 <https://doi.org/10.1016/j.epsl.2014.06.029>

654 Li, L., He, Y., Zhang, Z., Liu, Y., 2021a. Nitrogen isotope fractionations among gaseous and aqueous  
655  $\text{NH}_4^+$ ,  $\text{NH}_3$ ,  $\text{N}_2$ , and metal-ammine complexes: Theoretical calculations and applications.  
656 *Geochim. Cosmochim. Acta* 295, 80-97. <https://doi.org/10.1016/j.gca.2020.12.010>.

657 Li, Y.H., Li, L., Wu, Z.Q., 2021b. First-principles calculations of equilibrium nitrogen isotope  
658 fractionations among aqueous ammonium, silicate minerals and salts. *Geochim. Cosmochim.*  
659 *Acta* 297, 220-232. <https://doi.org/10.1016/j.gca.2021.01.019>

660 Li, L., Li, K., Li, Y., Zhang, J., Du, Y., Labbe, M., 2021 d. Recommendations on offline combustion-based  
661 nitrogen isotopic analysis of silicate minerals and rocks. *Rapid Commun. Mass Spectrom.*  
662 35(35), e9075. <https://doi.org/10.1002/rcm.9075>

663 Libourel, G., Marty, B., Humbert, F., 2003. Nitrogen solubility in basaltic melt. Part I. Effect of oxygen  
664 fugacity. *Geochim. Cosmochim. Acta* 67(21), 4123-4135. [https://doi.org/10.1016/S0016-7037\(03\)00259-X](https://doi.org/10.1016/S0016-7037(03)00259-X)

665

666 Liu, Y., Liu, X., Hu, Z., Diwu, C., Yuan, H., Gao, S., 2007. Evaluation of accuracy and long-term stability  
667 of determination of 37 trace elements in geological samples by ICP-MS. *Acta Petrologica Sinica*  
668 23(5), 1203-1210 (in Chinese with English abstract).

669 Mallik, A., Li, Y., Wiedenbeck, M., 2018. Nitrogen evolution within the Earth's atmosphere-mantle  
670 system assessed by recycling in subduction zones. *Earth Planet Sci. Lett.* 482, 556-566.  
671 <https://doi.org/10.1016/j.epsl.2017.11.045>

672 Marschall, H.R., Ludwig, T., Altherr, R., Kalt, A., Tonarini, S., 2006. Syros Metasomatic Tourmaline:  
673 Evidence for Very High- $\delta^{11}\text{B}$  Fluids in Subduction Zones. *J. Petrol.* 47(10), 1915-1942.  
674 <https://doi.org/10.1093/petrology/egl031>

675 Marschall, H.R., Schumacher, J.C., 2012. Arc magmas sourced from mélange diapirs in subduction zones.

676 Nat. Geosci. 5, 862-867. <https://doi.org/10.1038/ngeo1634>

677 Marty, B., Humbert, F., 1997. Nitrogen and argon isotopes in oceanic basalts. *Earth Planet Sci. Lett.*  
678 152(1), 101-112. [https://doi.org/10.1016/S0012-821X\(97\)00153-2](https://doi.org/10.1016/S0012-821X(97)00153-2)

679 Marty, B., Zimmermann, L., 1999. Volatiles (He, C, N, Ar) in mid-ocean ridge basalts: Assessment of  
680 shallow-level fractionation and characterization of source composition. *Geochim. Cosmochim.*  
681 *Acta* 63(21), 3619-3633. [https://doi.org/10.1016/S0016-7037\(99\)00169-6](https://doi.org/10.1016/S0016-7037(99)00169-6)

682 Marty, B., Dauphas, N., 2003. The nitrogen record of crust–mantle interaction and mantle convection  
683 from Archean to present. *Earth Planet Sci. Lett.* 206(3-4), 397-410.  
684 [https://doi.org/10.1016/S0012-821X\(02\)01108-1](https://doi.org/10.1016/S0012-821X(02)01108-1)

685 Melzer, S., Wunder, B., 2000. Island-arc basalt alkali ratios: Constraints from phengite-fluid partitioning  
686 experiments. *Geology* 28(7), 583-586. [https://doi.org/10.1130/0091-7613\(2000\)28](https://doi.org/10.1130/0091-7613(2000)28)

687 Ménez, B., Pasini, V., Brunelli, D., 2012. Life in the hydrated suboceanic mantle. *Nat. Geosci* 5(2), 133-  
688 137. <https://doi.org/10.1038/ngeo1359>

689 Mingram, B., Bräuer, K., 2001. Ammonium concentration and nitrogen isotope composition in  
690 metasedimentary rocks from different tectonometamorphic units of the European Variscan Belt.  
691 *Geochim. Cosmochim. Acta* 65(2), 273-287. [https://doi.org/10.1016/S0016-7037\(00\)00517-2](https://doi.org/10.1016/S0016-7037(00)00517-2)

692 Nielsen, S.G., Marschall, H.R., 2017. Geochemical evidence for mélange melting in global arcs. *Sci.*  
693 *Adv.* 3(4), e1602402. <http://10.1126/sciadv.1602402>

694 Pagé, L., Hattori, K., Guillot, S., 2018. Mantle wedge serpentinites: A transient reservoir of halogens,  
695 boron, and nitrogen for the deeper mantle. *Geology* 46(10), 883-886.  
696 <https://doi.org/10.1130/G45204.1>

697 Penniston-Dorland, S.C., Kohn, M.J., Manning, C.E., 2015. The global range of subduction zone thermal  
698 structures from exhumed blueschists and eclogites: Rocks are hotter than models. *Earth Planet*  
699 *Sci. Lett.* 428, 243-254. <https://doi.org/10.1016/j.epsl.2015.07.031>

700 Philippot, P., Busigny, V., Scambelluri, M., Cartigny, P., 2007. Oxygen and nitrogen isotopes as tracers  
701 of fluid activities in serpentinites and metasediments during subduction. *Mineral Petrol* 91(1-2),  
702 11-24. <https://doi.org/10.1007/s00710-007-0183-7>

703 Plank, T., Langmuir, C.H., 1998. The chemical composition of subducting sediment and its consequences  
704 for the crust and mantle. *Chem. Geol.* 145, 325-394. [https://doi.org/10.1016/S0009-2541\(97\)00150-2](https://doi.org/10.1016/S0009-2541(97)00150-2)

705

706 Plank, T., 2014. The chemical composition of subducting sediments. In: Keeling, R.F.E., Amsterdam  
707 (Ed.), *Treatise on Geochemistry*. Elsevier, pp. 607-629. <http://10.1016/B978-0-08-095975-7.00319-3>

708

709 Poli, S., Schmidt, M.W., 1995. H<sub>2</sub>O transport and release in subduction zones: Experimental constraints  
710 on basaltic and andesitic systems. *J. Geophys. Res. Solid Earth* 100(B11), 22299-22314.  
711 <https://doi.org/10.1029/95JB01570>

712 Sadofsky, S.J., Bebout, G.E., 2003. Record of forearc devolatilization in low-T, high-P/T  
713 metasedimentary suites: Significance for models of convergent margin chemical cycling.  
714 *Geochem. Geophys. Geosyst.* 4(4). <https://doi.org/10.1029/2002GC000412>

715 Sadofsky, S.J., Bebout, G.E., 2004. Nitrogen geochemistry of subducting sediments: New results from  
716 the Izu-Bonin-Mariana margin and insights regarding global nitrogen subduction. *Geochem.*  
717 *Geophys. Geosyst.* 5(3). <https://doi.org/10.1029/2003GC000543>

718 Saha, A., Basu, A.R., Wakabayashi, J., Wortman, G.L., 2005. Geochemical evidence for a subducted  
719 infant arc in Franciscan high-grade-metamorphic tectonic blocks. *GSA Bulletin* 117(9-10),



720 1318-1335. <https://doi.org/10.1130/B25593.1>

721 Sano, Y., Takahata, N., Nishio, Y., Fischer, T.P., Williams, S.N., 2001. Volcanic flux of nitrogen from the  
722 Earth. *Chem. Geol.* 171(3-4), 263-271. [https://doi.org/10.1016/S0009-2541\(00\)00252-7](https://doi.org/10.1016/S0009-2541(00)00252-7)

723 Schmidt, M.W., 1996. Experimental Constraints on Recycling of Potassium from Subducted Oceanic  
724 Crust. *Science* 272(5270), 1927-1930. <https://doi.org/10.1126/science.272.5270.1927>

725 Şengör, A.M.C., Natal'in, B.A., Burtman, V.S., 1993. Evolution of the Altaid tectonic collage and  
726 Palaeozoic crustal growth in Eurasia. *Nature* 364(6435), 299-307.  
727 <https://doi.org/10.1038/364299a0>

728 Shannon, R.T., Prewitt, C.T., 1969. Effective ionic radii in oxides and fluorides. *Acta Crystallographica*  
729 Section B: Structural Crystallography and Crystal Chemistry 25(5), 925-946.  
730 <https://doi.org/10.1107/S0567740869003220>

731 Sidey, V., 2016. On the effective ionic radii for ammonium. *Acta Crystallographica Section B: Structural*  
732 *Science, Crystal Engineering Materials* 72(4), 626-633.  
733 <https://doi.org/10.1107/S2052520616008064>

734 Sievers, N.E., Tenore, J., Penniston-Dorland, S.C., Bebout, G.E., 2017. Fingerprints of forearc element  
735 mobility in blueschist-facies metaconglomerates, Catalina Schist, California. *Int. Geol. Rev.*  
736 59(5-6), 741-752. <https://doi.org/10.1080/00206814.2016.1253038>

737 Sorensen, Sorena S., Grossman, J.N., Perfit, M.R., 1997. Phengite-hosted LILE Enrichment in Eclogite  
738 and Related Rocks: Implications for Fluid-Mediated Mass Transfer in Subduction Zones and  
739 Arc Magma Genesis. *J. Petrol.* 38(1), 3-34. <http://10.1093/petroj/38.1.3>

740 Spandler, C., Hermann, J., Faure, K., Mavrogenes, J.A., Arculus, R.J., 2008. The importance of talc and  
741 chlorite “hybrid” rocks for volatile recycling through subduction zones; evidence from the high-  
742 pressure subduction mélange of New Caledonia. *Contrib. Miner. Petrol.* 155(2), 181-198.  
743 <https://doi.org/10.1007/s00410-007-0236-2>

744 Staudigel, H., Plank, T., White, B., Schmincke, H.-U., 1996. Geochemical fluxes during seafloor  
745 alteration of the basaltic upper oceanic crust: DSDP Sites 417 and 418. *Subduction: top to*  
746 *bottom* 96, 19-38. <https://doi.org/10.1029/GM096p0019>

747 Staudigel, H., 2014. 4.16 - Chemical Fluxes from Hydrothermal Alteration of the Oceanic Crust. In:  
748 Holland, H.D., Turekian, K.K. (Eds.), *Treatise on Geochemistry* (second ed.). Elsevier, Oxford,  
749 pp. 583-606. <https://doi.org/10.1016/B978-0-08-095975-7.00318-1>

750 Sun, S.S., McDonough, W.F., 1989. Chemical and isotopic systematics of oceanic basalts: implications  
751 for mantle composition and processes. *Geol. Soc. Spec. Publ.* 42(1), 313-345.  
752 <https://doi.org/10.1144/GSL.SP.1989.042.01.19>

753 Tumiati, S., Godard, G., Martin, S., Malaspina, N., Poli, S., 2015. Ultra-oxidized rocks in subduction  
754 mélanges? Decoupling between oxygen fugacity and oxygen availability in a Mn-rich  
755 metasomatic environment. *Lithos* 226, 116-130. <https://doi.org/10.1016/j.lithos.2014.12.008>

756 Wang, J., Liu, X., 2016. Proficiency testing of the XRF method for measuring 10 major elements in  
757 different rock types. *Rock and Mineral Analysis* 35, 145-151 (in Chinese with English abstract).

758 Watenphul, A., Wunder, B., Wirth, R., Heinrich, W., 2010. Ammonium-bearing clinopyroxene: a  
759 potential nitrogen reservoir in the Earth's mantle. *Chem. Geol.* 270(1-4), 240-248.  
760 <https://doi.org/10.1016/j.chemgeo.2009.12.003>

761 Wu, F.Y., Yang, J.H., Lo, C.H., Wilde, S.A., Sun, D.Y., Jahn, B.M., 2007. The Heilongjiang Group: a  
762 Jurassic accretionary complex in the Jiamusi Massif at the western Pacific margin of  
763 northeastern China. *Island Arc* 16(1), 156-172. [24](https://doi.org/10.1111/j.1440-</a></p>
</div>
<div data-bbox=)



764 [1738.2007.00564.x](https://doi.org/10.1126/science.256.5053.80)

765 Xu, S., Su, W., Liu, Y., Jiang, L., Ji, S., Okay, A.I., Sengör, A.M.C., 1992. Diamond from the Dabie Shan  
766 metamorphic rocks and its implication for tectonic setting. *Science* 256(5053), 80-82.  
767 <https://doi.org/10.1126/science.256.5053.80>

768 Yamamoto, T., Nakahira, M., 1966. Ammonium ions in sericites. *American Mineralogist: Journal of*  
769 *Earth and Planetary Materials* 51(11-12), 1775-1778.

770 Ye, K., Cong, B., Ye, D., 2000. The possible subduction of continental material to depths greater than  
771 200 km. *Nature* 407(6805), 734-736. <https://doi.org/10.1038/35037566>

772 Zack, T., Rivers, T., Foley, S., 2001. Cs–Rb–Ba systematics in phengite and amphibole: an assessment  
773 of fluid mobility at 2.0 GPa in eclogites from Trescolmen, Central Alps. *Contrib. Mineral. Petrol.*  
774 140(6), 651-669. <https://doi.org/10.1007/s004100000206>

775 Zhou, J.B., Wilde, S.A., Zhang, X.Z., Zhao, G.C., Zheng, C.Q., Wang, Y.J., Zhang, X.H., 2009. The onset  
776 of Pacific margin accretion in NE China: evidence from the Heilongjiang high-pressure  
777 metamorphic belt. *Tectonophysics* 478(3-4), 230-246.  
778 <https://doi.org/10.1016/j.tecto.2009.08.009>

779 Zhou, J.B., Wilde, S.A., Zhao, G.C., 2010. New SHRIMP U-Pb Zircon Ages from the Heilongjiang  
780 Complex in NE China: Constraints on the Mesozoic Evolution of NE China. *Am. J. Sci.* 310,  
781 1024-1053. <https://doi.org/10.2475/09.2010.10>

782 Zhou, J.B., Han, J., Wilde, S., Guo, X., Zeng, W., Cao, J., 2013. A primary study of the Jilin-Heilongjiang  
783 high-pressure metamorphic belt: Evidence and tectonic implications. *Acta Petrol. Sin.* 29(2),  
784 386-398. <http://10.1016/j.sedgeo.2012.12.001>

785 Zhou, J.B., Cao, J.L., Wilde, S.A., Zhao, G.C., Zhang, J.J., Wang, B., 2014. Paleo-Pacific subduction-  
786 accretion: Evidence from Geochemical and U-Pb zircon dating of the Nadanhada accretionary  
787 complex, NE China. *Tectonics* 33(12), 2444-2466. <https://doi.org/10.1002/2014TC003637>

788 Zhou, J.B., Li, L., 2017. The Mesozoic accretionary complex in Northeast China: Evidence for the  
789 accretion history of Paleo-Pacific subduction. *J. Asian Earth Sci.* 145, 91-100.  
790 <https://doi.org/10.1016/j.jseaes.2017.04.013>

791 Zhu, C.Y., Zhao, G., Sun, M., Liu, Q., Han, Y., Hou, W., Zhang, X., Eizenhofer, P.R., 2015.  
792 Geochronology and geochemistry of the Yilan blueschists in the Heilongjiang Complex,  
793 northeastern China and tectonic implications. *Lithos* 216, 241-253.  
794 <https://doi.org/10.1016/j.lithos.2014.12.021>

795 Zhu, C.Y., Zhao, G., Sun, M., Eizenhöfer, P.R., Liu, Q., Zhang, X., Han, Y., Hou, W., 2017.  
796 Geochronology and geochemistry of the Yilan greenschists and amphibolites in the  
797 Heilongjiang complex, northeastern China and tectonic implications. *Gondwana Res.* 43, 213-  
798 228. <https://doi.org/10.1016/j.gr.2016.02.001>

799

## 1 **Figures captions**

2 Fig. 1. Geological sketch map of Northeast China (modified after Han et al., 2020). (a) Tectonic  
3 subdivisions of Northeast China showing multiple micro-continental blocks. (b) Map of the  
4 Jiamusi Block and adjacent areas showing the spatial distribution of the Heilongjiang Complex  
5 from the Mudanjiang area in the south, the Yilan area in the center, to the Luobei area in the  
6 north. The sample locations for this study are marked by stars. Abbreviations: F1 = the  
7 Mudanjiang Fault; F2 = the Yilan-Yitong Fault; F3 = the Dunhua-Mishan Fault; F4 = the  
8 Yuejinshan Fault; F5 = the Tanyuan-Xiguitu Fault; F6 = the Hegenshan-Heihe Fault; F7 = the  
9 Xar Moron-Changchun Fault.

10  
11 Fig. 2. Photographs of field outcrops and thin sections of blueschists from the Heilongjiang  
12 Complex. (a) outcrop of the Mudanjiang blueschist showing well-preserved pillow structure;  
13 (b) thin section of blueschist sample 15HLJ-05B from Mudanjiang (plane polarized light); (c)  
14 thin section of blueschist sample 15HLJ-01 from Mudanjiang (plane polarized light); (d)  
15 outcrop of the Yilan blueschist showing well-preserved pillow structure; (e) thin section of  
16 blueschist 15HLJ-39 from Yilan (plane polarized light); (f) thin section of blueschist 15HLJ-41  
17 from Yilan (plane polarized light). Abbreviations: Gl: glaucophane; Ab: albite; Ph: phengite;  
18 Ep: epidote; Ch: chlorite; Qtz: quartz.

19  
20 Fig. 3. Chondrite-normalized REE patterns for blueschists showing an affinity of enriched mid-  
21 ocean ridge basalts (E-MORB) for the Mudanjiang blueschists (a) and an affinity of ocean-  
22 island basalts (OIB) for the Yilan blueschists (b). The compositions of E-MORB and N-MORB  
23 are from Gale et al. (2013); and OIB from Sun and McDonough (1989).

24  
25 Fig. 4 Diagram showing the nitrogen concentrations and  $\delta^{15}\text{N}$  values of the blueschists from  
26 the Heilongjiang Complex in Northeast China. For comparison, the data of global altered  
27 oceanic crust (AOC), including Site 801 and 1149 (Li et al., 2007), Site 1256 (Bebout et al.,  
28 2018) and Site 504 (Busigny et al., 2019), are also shown. Compared with AOC ( $\text{N} < 19$  ppm),  
29 the blueschist samples are significantly more enriched in N, but show similar  $\delta^{15}\text{N}$  distribution  
30 patterns. The blueschist data can be interpreted by mixing of two types of ammonium: one with  
31  $\delta^{15}\text{N}$  value of +3‰, and the other with  $\delta^{15}\text{N}$  value of  $\sim -16$ ‰. Numbers along the curves mark  
32 the fractions of added ammonium by increment of 10%. See text for detailed discussion. **Note**  
33 **that, on x-axis, N concentration is plotted in logarithmic scale from 1 ppm to 19 ppm and non-**  
34 **logarithmic scale from 19 ppm to 150 ppm. The vertical grey dashed line marks the N**  
35 **concentration of 19 ppm.** The error bars of N concentrations and  $\delta^{15}\text{N}$  values are smaller than  
36 the symbols and not shown in the diagram.

37  
38 Fig. 5. Comparison of N concentrations with the concentrations of  $\text{K}_2\text{O}$  (a),  $\text{Na}_2\text{O}$  (b) and  $\text{MgO}$   
39 (c). Positive correlation is only observed between N and  $\text{K}_2\text{O}$  concentrations. This suggests that  
40 nitrogen (in form of  $\text{NH}_4^+$ ) is primarily resided in K-bearing minerals (i.e., phengite in  
41 blueschists), rather than Na- or Ca-bearing minerals.

43 Fig. 6. Diagrams comparing the molar abundances of Rb, Cs, K, N and  $\delta^{15}\text{N}$  values of the  
44 blueschists to infer the devolatilization effect. In panels a and b, the solid blue and black lines  
45 are linear fittings of the Mudanjiang and Yilan blueschist data (note that one outlier from Yilan  
46 group A blueschists obviously falling outside the other datasets in Fig. 6a was excluded for liner  
47 fitting); grey dashed curves represent the devolatilization trends modeled by Equation (1) for  
48 Mudanjiang and Yilan blueschist data. Numbers along the curves are the fractions of elemental  
49 loss after devolatilization. In panel c, the lack of negative correlations between the N/K molar  
50 ratios and  $\delta^{15}\text{N}$  values suggests that the effect of metamorphic devolatilization on N is minor.  
51

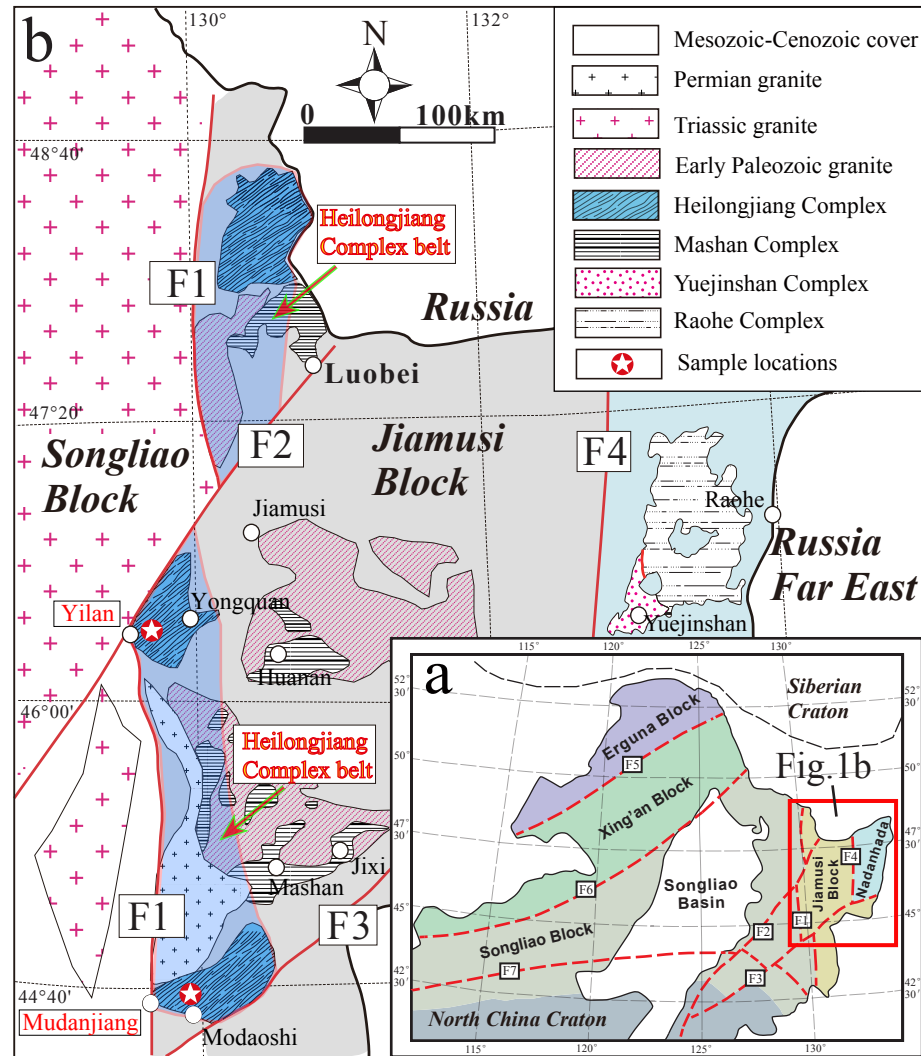
52 Fig. 7 Diagrams showing the different effects of low-temperature seafloor alteration and  
53 subduction-zone metamorphism on (a) K and Ba concentrations (both normalized to Th  
54 concentration) and (b) Th/U ratios and Th concentrations. The seafloor alteration effect trends  
55 (grey arrows) are defined by the data of modern altered oceanic crust (AOC), including ODP  
56 sites 801 and 1149 (Kelley et al., 2003), Site 801 (Kelley et al., 2003) and Site 504 (Bach et al.,  
57 2003). The subduction-zone metamorphic effects (pink arrows) are defined by high-grade  
58 eclogites from the Raspas Complex (Eclogites-1) (John et al., 2004; Halama et al., 2010) and  
59 Samana Peninsula (Eclogites-2) (Sorensen et al., 1997). The compositions of E-MORB and N-  
60 MORB (Gale et al., 2013) and OIB (Sun and McDonough, 1989) are also plotted for reference.  
61 The blueschists from the Heilongjiang Complex show trends distinct to the seafloor alteration  
62 effect but consistent with the subduction-zone metamorphic effect.  
63

64 Fig. 8. Correlations of N concentrations with Ba concentrations (a) and Th concentrations (b)  
65 of the blueschists from the Heilongjiang Complex. The solid lines are linear regressions for the  
66 Mudanjiang blueschists and the Yilan-group A blueschists (see text for discussion).  
67

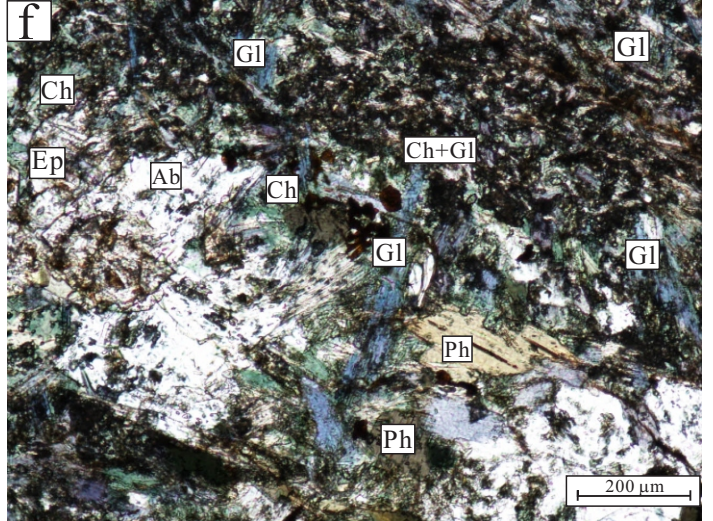
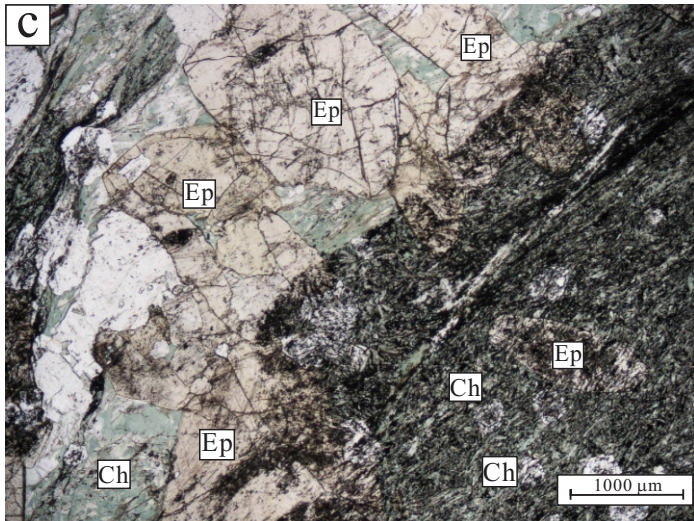
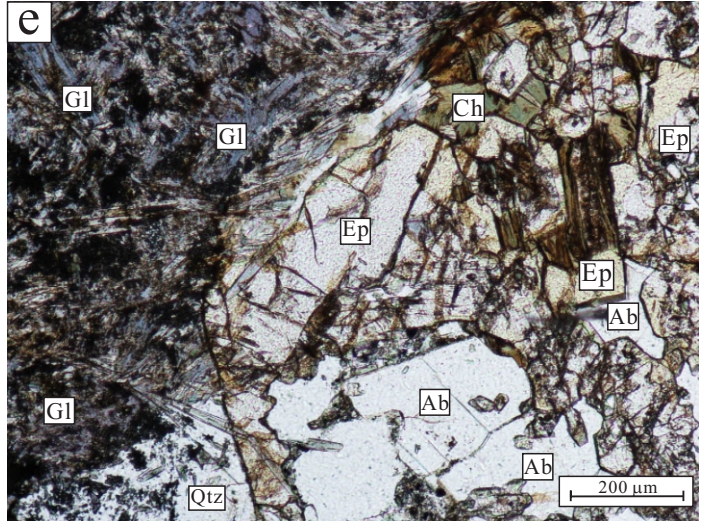
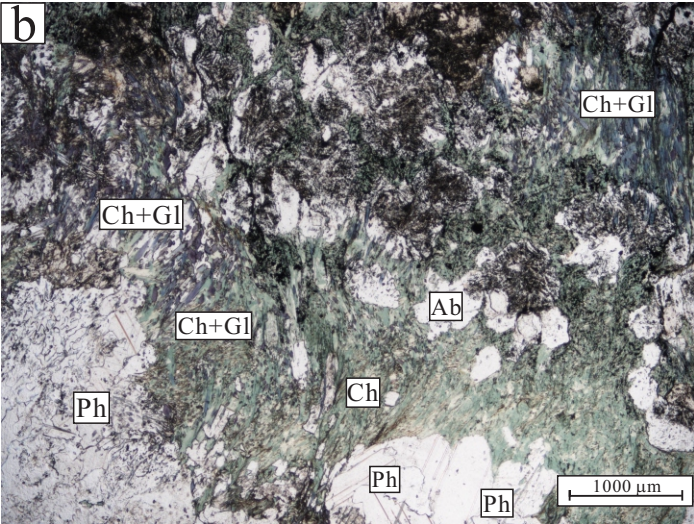
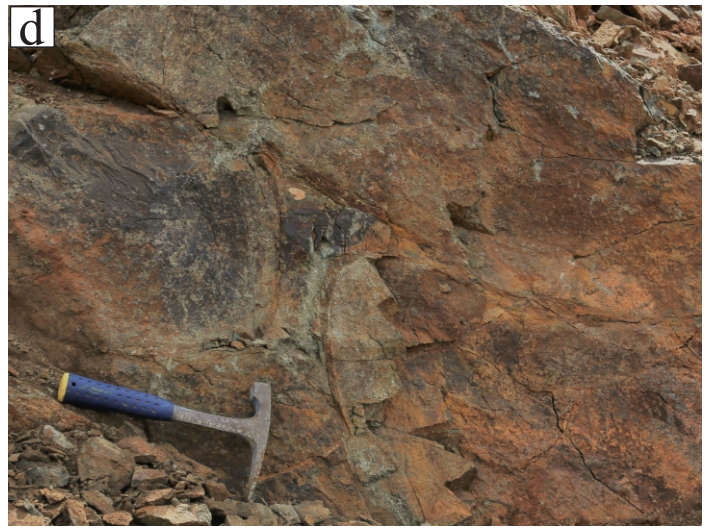
68 Fig. 9. Schematic diagram (not to scale) showing the N transfer from the sedimentary  
69 components to the meta-igneous components in the mélange of a subduction zone (modified  
70 from Bebout and Penniston-Dorland, 2016). Two N transfer pathways are illustrated in the  
71 diagram. One is that N is released from sediments as  $\text{NH}_4^+$ , which is subsequently re-fixed by  
72 the meta-igneous components through fluid-rock interaction. The other is that N is released  
73 from sediments as  $\text{N}_2$ , which is reduced into  $\text{NH}_4^+$  and subsequently re-fixed by the meta-  
74 igneous components.  
75

76 Fig. 10. Diagram showing the relationship between the N re-fixation efficiency and the  
77 thickness of sediments and altered oceanic crust (AOC) that are incorporated into the mélange.  
78 The numbers on the curves represent the thickness of AOC. The parameters used in the  
79 modeling include average density ( $1.64 \text{ g/cm}^3$ ) and porosity (38.5%) of subducting sediments  
80 from Plank and Langmuir. (1998), average density ( $2.93 \text{ g/cm}^3$ ) and porosity (12%) of  
81 subducting AOC from Johnson and Pruis (2003), the initial weighted average N concentrations  
82 of 299 ppm for sediments (Sadofsky and Bebout, 2004; Li and Bebout, 2005) and 7 ppm for  
83 AOC (Busigny et al., 2005, 2019; Li et al., 2007; Bebout et al., 2018), and the final average N  
84 concentration of 51 ppm (this study) for the blueschist-facies igneous rocks. The horizontal  
85 grey bar represents the maximum fraction of N loss of sediments during the early-stage  
86 subduction. The vertical grey bar represents the average thickness of the subducting sediments

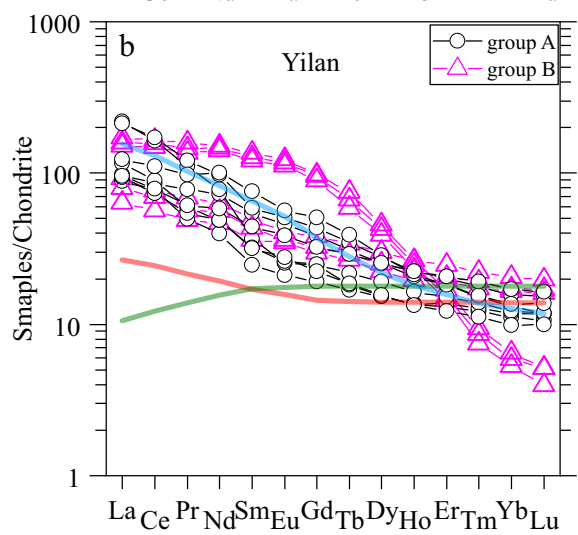
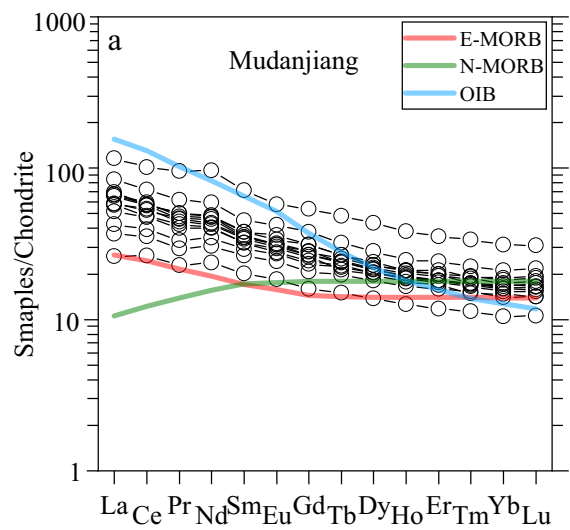
87 along the Circum-Pacific subduction zones (Plank and Langmuir, 1998; Clift, 2017). The  
88 python code for modeling is available at [https://github.com/GeoCan22/N-Re-fixation-](https://github.com/GeoCan22/N-Re-fixation-Efficiency-Modeling)  
89 [Efficiency-Modeling](https://github.com/GeoCan22/N-Re-fixation-Efficiency-Modeling)

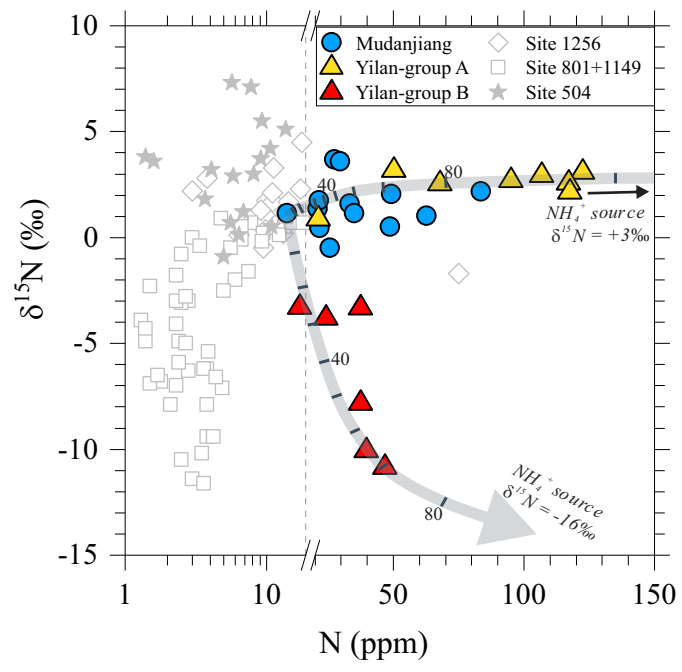




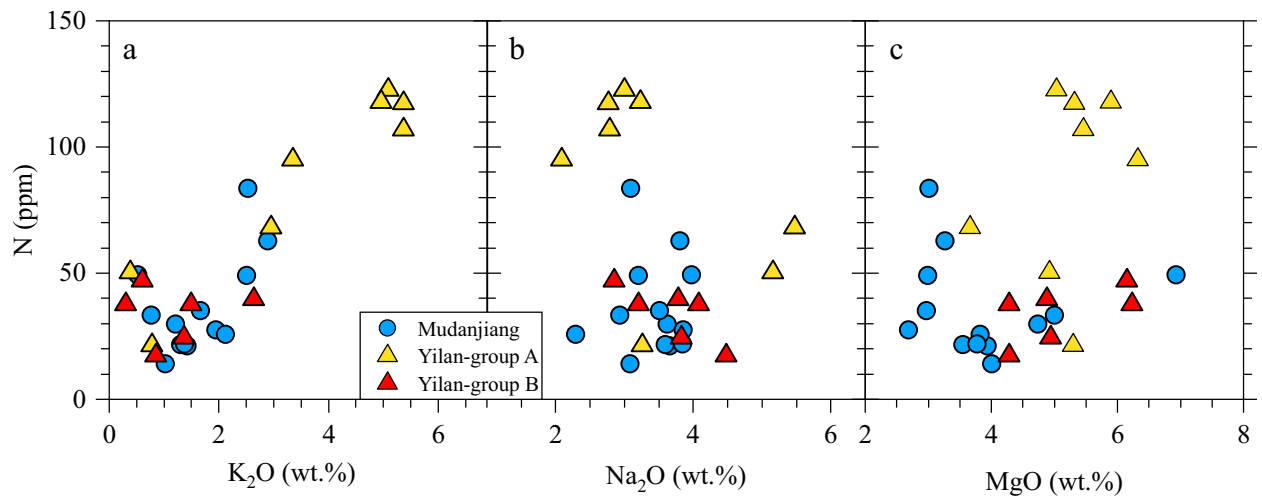


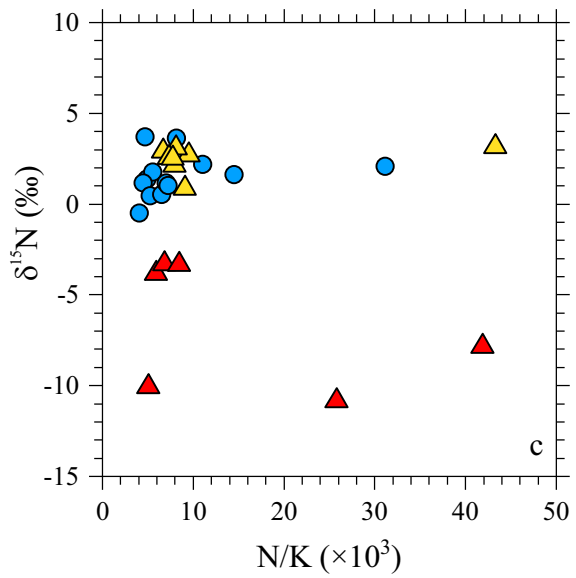
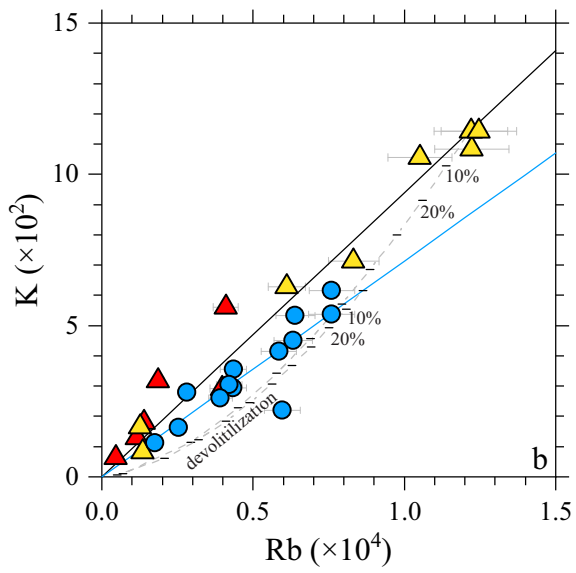
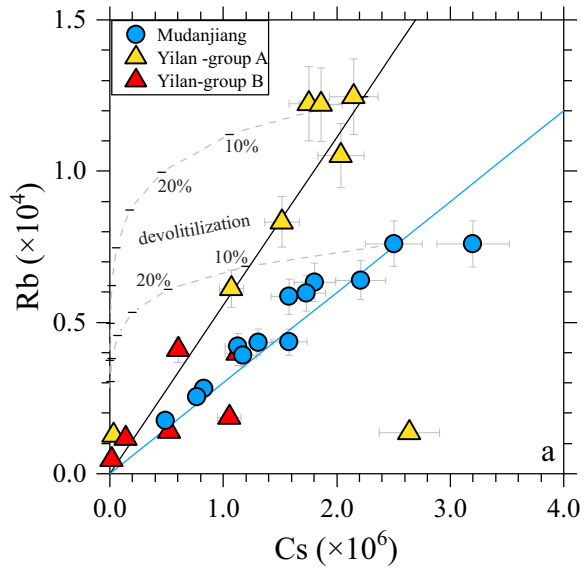


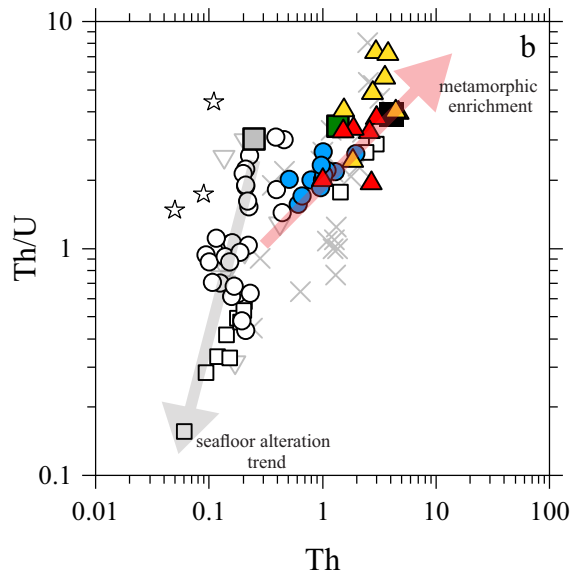
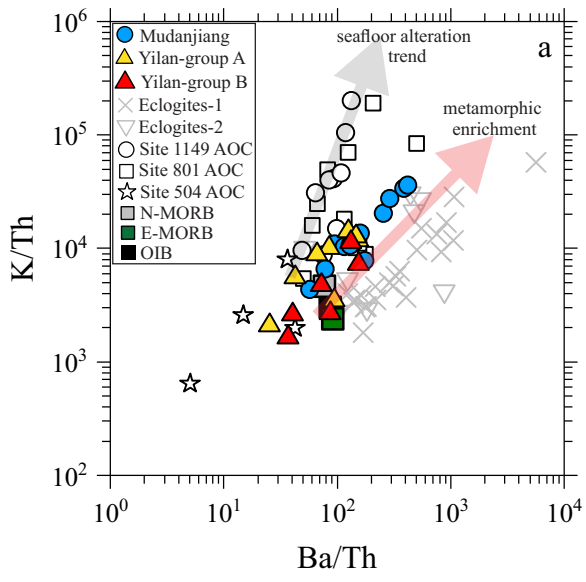


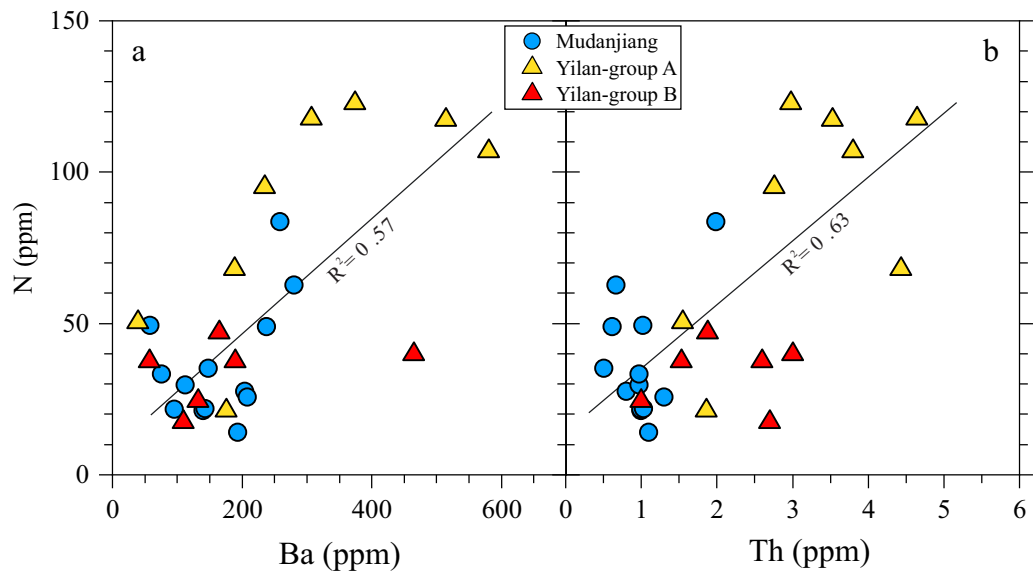


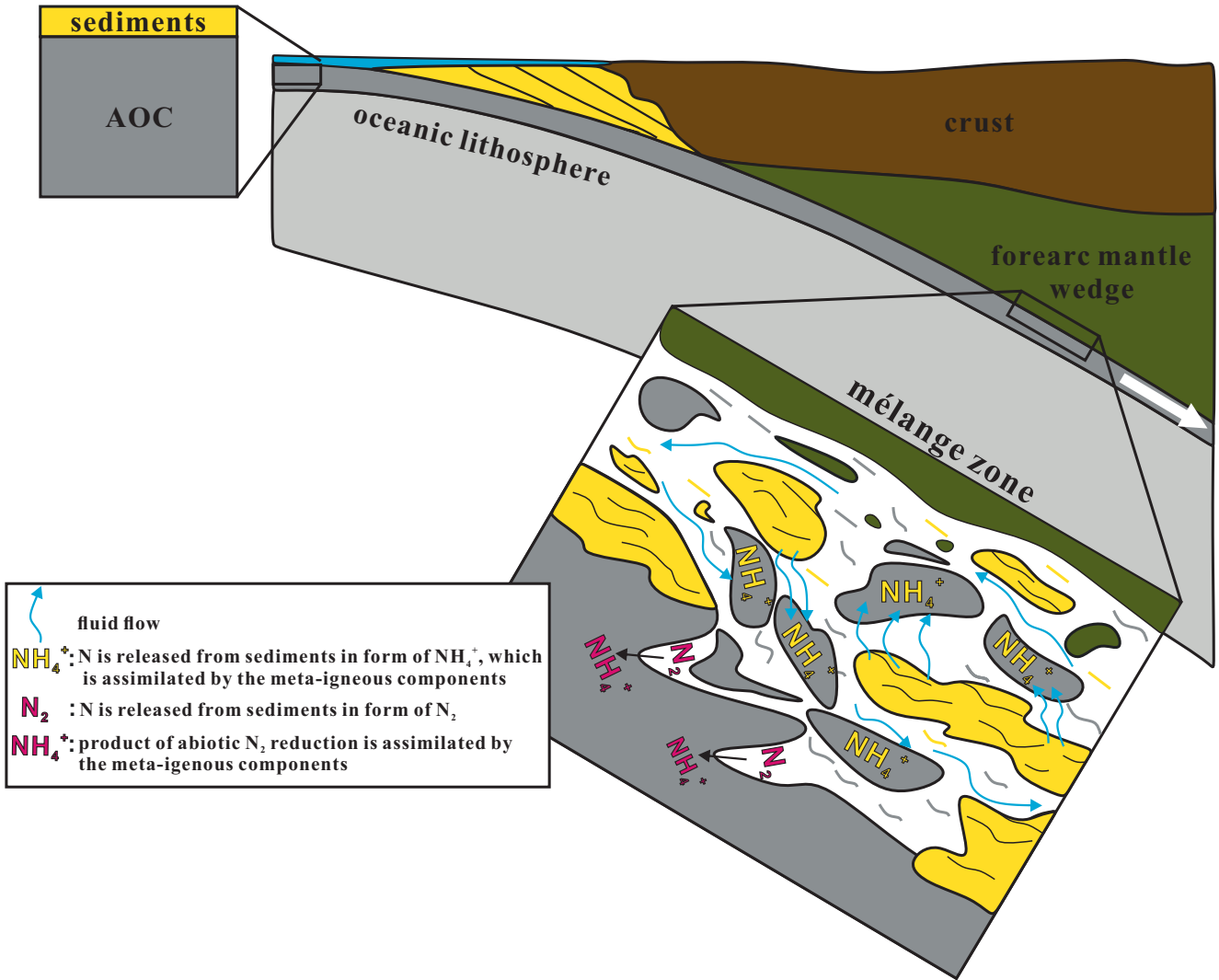












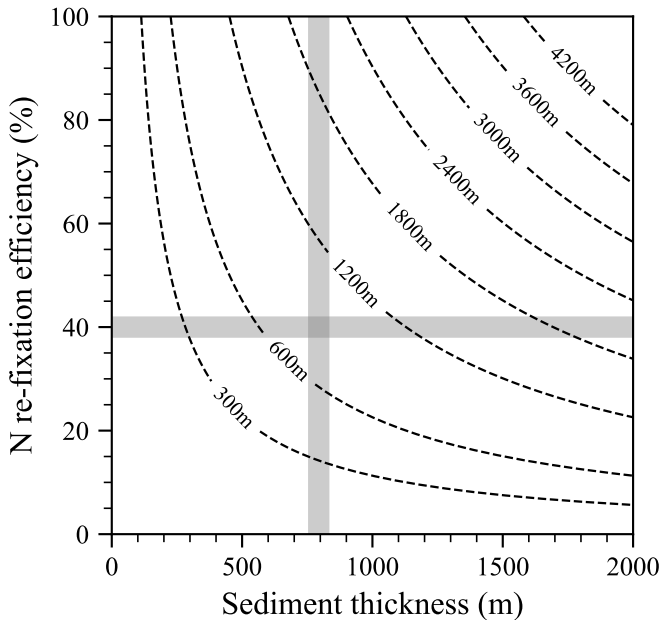


Table1. N concentrations,  $\delta^{15}\text{N}$  values, major and trace element compositions of blueschists from Heilongjiang Complex, Northeast China.

	Mudanjiang blueschists												
	20HLJ-14	20HLJ-14-1	20HLJ-14-2	20HLJ-14-3	20HLJ-15	20HLJ-15-1	20HLJ-15-2	20HLJ-15-3	15HLJ-06	15HLJ-02	15HLJ-05B	15HLJ-01	15HLJ-04
SiO <sub>2</sub>	45.22	44.21	44.37	42.78	43.65	44.73	46.65	43.15	44.75	45.1	42.87	45.29	40.01
TiO <sub>2</sub>	2.48	2.33	2.47	2.24	1.98	1.57	2.06	3.20	1.971	2.105	2.715	2.15	2.368
Al <sub>2</sub> O <sub>3</sub>	16.36	15.98	15.85	15.61	17.20	13.96	18.43	15.79	14.21	16.27	17.24	16.77	15.51
TFe <sub>2</sub> O <sub>3</sub>	12.46	12.91	11.76	11.91	12.90	11.41	12.98	14.95	11.3	13.23	15.37	12.36	12.21
MnO	0.12	0.17	0.12	0.23	0.10	0.11	0.08	0.11	0.128	0.144	0.144	0.159	0.178
MgO	3.78	6.93	4.74	5.00	2.99	2.97	3.27	3.02	2.69	3.94	3.83	3.55	4.01
CaO	8.92	7.01	9.38	11.63	9.10	11.05	5.48	8.26	12.6	9.24	9.64	10.49	14.47
Na <sub>2</sub> O	3.85	3.98	3.62	2.94	3.21	3.51	3.81	3.09	3.86	3.66	2.29	3.6	3.08
K <sub>2</sub> O	1.38	0.53	1.22	0.77	2.51	1.67	2.89	2.53	1.95	1.43	2.12	1.31	1.03
P <sub>2</sub> O <sub>5</sub>	0.39	0.37	0.36	0.35	0.27	0.29	0.31	0.62	0.31	0.38	0.36	0.52	0.37
LOI	4.61	5.19	5.75	6.51	5.75	8.30	3.73	5.07	5	2.9	3.37	4.09	7.12
Total	99.57	99.61	99.64	99.97	99.66	99.57	99.69	99.79	98.77	98.4	99.94	100.3	100.3
Li (ppm)	23.0	37.1	24.5	28.4	33.4	29.1	34.9	32.0	n.a	n.a	n.a	n.a	n.a
Be	1.28	1.07	1.46	1.02	1.20	0.81	1.35	1.94	2	1	1	1	<1
Sc	31.6	29.7	27.0	26.3	33.7	25.9	32.9	31.9	24	28	31	27	27
V	214	197	207	220	247	199	259	300	204	203	277	231	214
Cr	224	226	219	224	111	98.4	105	164	190	210	270	220	230
Co	41.7	90.6	67.2	75.1	43.0	70.6	60.4	50.6	25	46	42	40	52
Ni	147	212	180	213	122	119	118	123	100	150	140	160	170
Cu	49.4	58.9	71.2	65.6	50.3	51.0	42.9	50.7	40	40	50	50	40
Zn	98.7	135	110	105	89.2	90.5	97.2	112	70	110	120	90	120
Ga	15.4	18.1	15.7	20.2	16.8	13.3	17.4	24.6	12	16	20	18	17
Ge	1.33	1.36	1.33	1.74	1.28	0.97	1.20	2.43	<1	1	2	2	1
Rb	37.1	15.1	33.5	21.7	54.7	37.2	65.0	64.9	50	36	54	34	24
Sr	235	212	248	412	234	185	164	314	204	212	281	281	371
Y	33.2	29.7	29.4	32.3	26.1	19.1	28.4	58.3	25	30	36	30	29
Zr	184	182	182	168	123	95.3	131	320	153	161	214	165	183
Nb	18.6	19.2	19.0	17.7	10.4	7.98	11.2	30.9	14	15	20	17	17
Cs	1.74	0.65	1.56	1.02	2.94	2.10	3.33	4.25	2.1	1.5	2.4	1.5	1.1
Ba	143	58.6	113	76.1	238	148	280	259	204	140	208	132	96
La	16.0	13.8	12.3	15.5	8.75	6.20	10.1	27.5	13.5	16.4	19.9	15	13.8
Ce	36.1	33.0	29.1	34.7	21.7	16.2	24.0	62.1	29.6	35	44.3	34.7	32.4
Pr	4.56	4.19	3.82	4.43	2.80	2.16	3.16	9.12	4.04	4.77	5.87	4.64	4.38
Nd	22.1	19.9	18.7	21.4	14.3	11.1	16.2	44.8	19	22.7	27.6	21.8	20.3
Sm	5.51	5.22	4.89	5.38	4.03	3.09	4.45	10.9	4.9	5.8	6.9	5.5	5.3
Eu	1.80	1.76	1.60	1.82	1.40	1.07	1.57	3.34	1.71	1.95	2.44	2.01	1.84
Gd	5.73	5.48	5.03	5.47	4.27	3.29	4.80	11.0	5.3	6.4	7.8	6.1	5.8
Tb	0.94	0.89	0.84	0.90	0.74	0.56	0.83	1.81	0.8	1	1.2	1	0.9
Dy	5.77	5.45	5.20	5.60	4.61	3.50	5.15	11.1	5	5.8	7.2	5.7	5.4
Ho	1.19	1.09	1.06	1.14	0.94	0.71	1.06	2.16	1	1.2	1.4	1.1	1.1
Er	3.31	2.98	2.98	3.20	2.63	1.95	2.90	5.87	2.8	3.3	4	3.2	3
Tm	0.49	0.43	0.44	0.48	0.39	0.29	0.42	0.86	0.38	0.44	0.57	0.44	0.44
Yb	3.10	2.71	2.72	2.96	2.38	1.79	2.61	5.27	2.5	2.8	3.6	2.8	2.9
Lu	0.48	0.40	0.42	0.46	0.36	0.27	0.39	0.78	0.36	0.44	0.55	0.41	0.42
Hf	4.10	3.93	4.05	3.73	2.98	2.32	3.21	7.36	3.4	3.9	4.9	3.8	4.1
Ta	1.20	1.20	1.22	1.15	0.67	0.56	0.73	1.97	0.9	1	1.4	1.1	1.1
Pb	0.77	0.80	0.84	1.56	0.59	0.43	0.82	1.78	<5	<5	<5	<5	<5
Th	1.03	1.02	0.98	0.97	0.62	0.51	0.67	1.99	0.8	1	1.3	1	1
U	0.49	0.38	0.42	0.52	0.39	0.25	0.39	0.76	0.4	0.5	0.6	0.5	0.5
N (ppm)	21.9	49.2	29.7	33.3	48.9	35.0	62.6	83.6	27.5	21.1	25.6	21.6	13.9
$\delta^{15}\text{N}$ (‰)	0.5	2.1	3.6	1.6	0.5	1.2	1.0	2.2	3.7	1.4	-0.5	1.7	1.1

Yilan blueschists														
	19HLJ-04	19HLJ-07	19HLJ-08	19HLJ-09	19HLJ-10	19HLJ-11	19HLJ-12	20HLJ-31-1	20HLJ-31-2	20HLJ-31-3	15HLJ-38	15HLJ-39	15HLJ-40	15HLJ-41
SiO <sub>2</sub> (wt.%)	47.34	39.86	52.32	51.08	51.10	50.64	50.32	47.31	45.84	45.67	46.04	47.24	45.49	45.63
TiO <sub>2</sub>	2.64	2.50	3.26	2.69	2.93	2.97	2.86	2.89	1.96	2.92	4.556	3.465	3.303	3.126
Al <sub>2</sub> O <sub>3</sub>	14.91	11.28	13.79	14.58	14.86	13.46	13.14	14.63	13.30	18.51	12.59	12.35	12.21	13.16
TFe <sub>2</sub> O <sub>3</sub>	12.66	10.82	12.55	11.30	11.51	12.01	13.93	13.12	9.58	10.85	15.91	15.31	13.02	13.43
MnO	0.19	0.22	0.07	0.11	0.08	0.10	0.07	0.16	0.14	0.13	0.132	0.109	0.125	0.125
MgO	6.15	6.32	5.04	5.46	5.32	5.90	3.66	6.23	4.92	5.30	4.94	4.88	4.28	4.28
CaO	9.00	11.92	1.89	3.06	2.30	2.25	3.44	8.41	10.10	8.00	7.62	5.26	10.31	9.63
Na <sub>2</sub> O	2.85	2.09	3.00	2.79	2.77	3.23	5.48	3.21	5.16	3.26	3.83	3.78	4.48	4.08
K <sub>2</sub> O	0.61	3.35	5.09	5.37	5.37	4.96	2.95	0.30	0.39	0.78	1.37	2.64	0.85	1.49
P <sub>2</sub> O <sub>5</sub>	0.47	0.72	0.22	0.25	0.32	0.82	1.90	0.35	0.34	0.36	0.85	1.25	1.25	1.22
LOI	2.89	11.15	2.77	3.50	3.49	3.62	2.15	3.12	7.96	3.94	2.7	2.77	3.49	4.4
Total	99.71	100.23	100.00	100.19	100.05	99.96	99.90	99.73	99.69	99.72	100.5	99.06	98.81	100.6
Li (ppm)	19.9	30.3	34.3	31.8	36.6	36.8	21.4	8.84	35.7	11.6	n.a	n.a	n.a	n.a
Be	1.47	1.46	1.67	2.11	2.06	1.99	1.53	1.60	1.31	0.88	3	4	3	3
Sc	29.5	19.1	20.3	18.6	19.2	15.1	15.1	35.7	14.6	35.7	9	6	6	6
V	245	122	92.1	78.4	109	92.4	90.9	306	131	256	232	176	164	157
Cr	148	19.5	40.4	28.3	34.3	12.5	9.43	155	138	44.3	30	50	50	50
Co	42.5	27.2	31.6	27.9	28.3	17.7	11.6	51.3	51.6	45.4	46	34	44	35
Ni	94.4	24.6	44.3	38.2	43.4	11.6	9.12	64.7	133	32.6	90	70	90	60
Cu	58.3	12.4	13.6	11.7	12.4	12.6	11.8	85.5	104	72.1	10	< 10	10	20
Zn	108	125	128	116	105	137	95.3	111	79.3	88.3	240	240	230	210
Ga	21.6	16.5	19.3	20.9	21.5	20.4	14.4	20.8	11.2	22.0	39	41	40	36
Ge	1.52	1.44	1.70	1.64	1.74	1.58	1.37	1.46	1.37	1.33	1	1	1	1
Rb	9.86	71.1	105	104	106	89.9	52.2	3.95	11.5	10.9	16	35	12	16
Sr	219	592	15.9	61.7	45.8	58.6	111	371	186	494	691	368	970	1024
Y	40.5	32.6	17.6	17.4	22.2	32.2	29.1	33.8	20.9	34.5	39	38	35	33
Zr	218	149	190	219	225	265	253	192	103	200	428	515	500	475
Nb	24.4	38.4	39.4	43.1	45.4	68.6	68.0	22.0	32.4	28.0	26	33	30	29
Cs	0.19	2.02	2.33	2.48	2.86	2.70	1.42	0.025	3.51	0.049	< 0.5	0.8	0.7	1.4
Ba	164	235	374	581	514	308	188	56.8	39.1	175	227	465	110	190
La	21.8	23.2	21.0	51.8	27.4	50.2	29.2	18.8	22.3	22.6	39.8	40.5	37.7	35.7
Ce	47.0	51.8	47.4	100	54.7	105	67.5	42.3	44.8	47.9	101	101	95.8	90.9
Pr	6.55	7.38	4.74	10.5	5.62	11.4	9.27	5.35	5.14	5.78	14.7	15	13.8	12.9
Nd	29.7	34.0	18.5	36.4	22.7	45.5	46.8	26.1	22.7	27.1	75.8	70.8	68.6	65.8
Sm	7.59	8.33	3.77	5.65	4.92	8.96	11.5	6.63	4.86	6.76	21.7	20.7	19.3	18.5
Eu	2.36	2.64	1.23	1.47	1.51	2.94	3.28	2.09	1.60	2.23	8.13	7.16	6.77	6.49
Gd	7.87	7.91	3.93	5.05	5.11	8.90	10.4	6.68	4.62	6.68	23.9	20	19.6	18.4
Tb	1.28	1.16	0.63	0.68	0.82	1.30	1.46	1.08	0.70	1.09	2.8	2.8	2.5	2.2
Dy	7.62	6.41	3.87	3.90	4.84	7.04	7.26	6.40	3.98	6.45	12.1	11.6	10.8	9.9
Ho	1.49	1.17	0.77	0.77	0.93	1.26	1.21	1.26	0.76	1.27	1.6	1.5	1.4	1.3
Er	4.08	2.99	2.15	2.27	2.51	3.35	3.02	3.39	2.01	3.42	2.9	2.8	2.5	2.4
Tm	0.56	0.39	0.31	0.32	0.35	0.45	0.39	0.49	0.29	0.49	0.26	0.24	0.22	0.19
Yb	3.49	2.23	1.88	2.01	2.09	2.65	2.32	2.92	1.69	2.90	1.2	1.1	1	0.9
Lu	0.50	0.30	0.27	0.30	0.30	0.39	0.35	0.43	0.25	0.42	0.14	0.13	0.13	0.1
Hf	5.13	3.71	4.58	5.20	5.42	6.17	5.94	4.68	2.49	4.71	11.4	12.4	11.2	10.8
Ta	1.50	1.95	2.53	2.70	2.86	3.69	3.24	1.35	1.83	1.66	1.7	2.1	2	1.9
Pb	1.78	5.83	1.12	1.18	1.19	1.22	1.32	2.17	4.14	2.53	< 5	< 5	< 5	< 5
Th	1.88	2.76	2.98	3.80	3.53	4.64	4.44	1.53	1.55	1.87	2.1	3	2.7	2.6
U	0.56	0.57	0.41	0.53	0.62	1.18	1.11	0.47	0.38	0.77	0.8	0.8	1.4	0.8
N (ppm)	46.9	95.0	122.6	106.9	117.2	117.7	67.9	37.4	50.29	21.20	24.3	39.7	17.3	37.5
δ <sup>15</sup> N (‰)	-10.9	2.7	3.1	2.9	2.6	2.1	2.5	-7.8	3.2	0.9	-3.8	-10.1	-3.3	-3.3

n.a. data not analyzed.



Table 2. Exchange coefficients and initial elemental ratios employed in the progressive devolatilization modeling.

	$K_D$	$R_{rock}^0$
Rb-K	1.62 <sup>a</sup>	0.11 <sup>b</sup>
Cs-Rb	0.14 <sup>a</sup>	1.80 <sup>b</sup>

- a. The  $K_D$  values of Rb-K and Cs-Rb between phengite and fluid at 600 °C, 2GPa were used.
- b. The highest molar abundances of K ( $\times 10^2$ ), Rb ( $\times 10^4$ ) and Cs ( $\times 10^6$ ) in each location were employed as their initial molar abundances to derive the initial elemental ratios.